Response to Reviewer 1 Queries/Comments

Citation: https://doi.org/10.5194/egusphere-2026-363-RC1

Dear Editor and Reviewer,

We appreciate you taking the time to provide us with all of your insightful and valuable comments and recommendations. All of them have been carefully considered, and we have made a concerted effort to answer them all in detail. Your unaltered original remarks are written in **grey** in this response, while our responses are written in **blue**. Certain key highlights in some of the responses have been emphasized using **bold text**.

General Comments:

Tiwari et al. derive the clear sky TOA direct radiative forcing due to black carbon (BCTOA DRF) using the outputs from the COSMO framework (their previous work) constrained by multi-spectral spaceborne AOD retrievals, and then employing SBDART model for BCTOA DRF calculation, for two geographical regions: Xuzhou and Dhaka. The BCTOA DRF estimated using SBDART is then used to train statistical ML model, whose efficacy is discussed in the manuscript for various microphysical properties (including amount) of BC. Shapley values were used to determine the contribution of different predictors in ML prediction of BCTOA DRF. The datasets used in this study, along with the methodology, are clearly described and well justified. The manuscript is well written and easy to follow. I have a few minor comments that aim to further improve the manuscript.

We sincerely thank the reviewer for the encouraging and constructive evaluation of our manuscript. We are grateful that the reviewer found the dataset selection, methodological framework, and scientific presentation to be clear, well justified, and easy to follow. In response to the comments, we made the following revisions to improve clarity, reproducibility, and figure presentation:

- **Methodological clarification:** Clarified how BC TOA DRF is calculated using COSMO-derived microphysical/optical properties and SBDART, added references for AOD–flux approaches, and specified the observational requirements for extending the framework to other AERONET/SONET sites.
- **ML-model transparency:** Defined the predictor variables, statistical metrics, Random Forest configuration, hyperparameters, and the rationale for comparing Linear, MLR, and ML models as a complexity gradient for BC TOA prediction.
- **Figure/text improvements:** Corrected figure labels, increased font sizes, reorganized crowded panels into the Supplement, added explicit panel references throughout the Results

We appreciate the comments provided, which have helped us improve the clarity, consistency, and presentation of the manuscript. All comments have been carefully considered and addressed in the revised version, as described in detail in the point-by-point responses below.

Minor comments:

Line 67: Are there any valid references which use linear AOD-flux relationship?

Thank you for this comment. We agree and have supported this statement with references at its first occurrence in the Introduction. Relevant examples of linear or radiative-efficiency-type AOD-TOA forcing approximations were cited in Section 2.2, where we discuss the linear surrogate model and the common practice of representing TOA forcing as a function of AOD. In the revised manuscript, we have now introduced these and additional references at Line 68.

The central idea in these approaches is that TOA shortwave flux or TOA aerosol forcing is empirically related to AOD, either through a regression between coincident satellite-retrieved AOD and TOA flux, or through a radiative-forcing-efficiency formulation in which the slope represents the TOA radiative response per unit aerosol loading. More recent examples like He et al. (2017) estimated TOA instantaneous aerosol direct radiative effects over the Yangtze River Basin using a linear relationship between CERES shortwave upward flux and coincident MODIS AOD550. Similarly, Biswas et al. (2017) estimated aerosol-free TOA flux over North-East India from a linear regression between CERES shortwave TOA fluxes and MODIS AOD, with the regression intercept representing the zero-AOD reference condition. These are directly adapted from Christopher and Zhang (2002) which used cloud-free, very low-AOD CERES-MODIS pixels to represent non-aerosol conditions when estimating shortwave aerosol radiative forcing over oceans. These examples support the statement that empirical AOD-flux or low-AOD reference approaches have been used in aerosol science community for aerosol forcing estimatation.

This is also why we include a linear benchmark model in our study: to evaluate how well traditional first-order BCAOD550-BCTOA approximation performs relative to the more physically informed MLR and ML models that include BC column loading and microphysical state.

Revised Manuscript text:

"*Furthermore, computing no-aerosol fluxes to derive net TOA forcing adds to the existing challenge. Studies often assume either linear AOD-flux relationships (computing* $TOA_{no\text{-}aerosol\text{-}flux}$ *at AOD =0) or using low-aerosol pixels for pristine flux (Biswas et al., 2017; Christopher and Zhang, 2002; Sundström et al., 2015).*"

Line 95: How is the BCTOA DRF calculated from TOA fluxes? The values reported in the results are strongly negative compared to the global mean low positive values reported in previous studies, also stated in lines 44 and 45 of the manuscript.

The adapted approach to compute BCDRF follows a sequence of: (a) observationally constrained optical property derivation, followed by (b) spatio-temporally hamonizing ancillary

datasets from multiple observation platrforms, and (c) simulation using these results and properties of (a) and (b) in the radative transfer model.

As discussed in the Introduction, estimating aerosol-type-specific forcing directly from satellite-observed TOA fluxes remains challenging because the observed flux contains the combined radiative influence of all aerosol species. Therefore, isolating the BC-specific contribution from observed TOA fluxes would require additional assumptions regarding aerosol composition, mixing state, vertical distribution, and the aerosol-free reference state.

In this study, we instead use an observation-constrained radiative transfer approach. First, we derive an ensemble of BC-containing aerosol microphysical states using the COSMO core–shell Mie framework. The BC core size and sulfate-shell size combinations are constrained by multi-waveband SSA from TROPOMI and AERONET/SONET, while accounting for cross-platform uncertainty and wavelength offsets. Only size/mixing-state combinations that reproduce the uncertainty-bounded SSA constraints across all wavelengths are retained. Second, these retained microphysical solutions are used to compute the aerosol optical properties required by the radiative transfer model. Specifically, BCAOD is calculated from the constrained core-shell size, particle density, extinction efficiency, mass extinction efficiency, and column mass density. The resulting BCAOD is then further screened using yet additional observational constraints: modeled BCAOD must remain below the observed total AOD upper bound at all of 388 nm, 470 nm, and 550 nm. Cases violating this column-feasibility condition at any wavelength are removed.

The final constrained aerosol optical properties, namely BCAOD, SSA, and ASY at 388, 470, and 550 nm, are then provided to SBDART together with satellite-derived ancillary inputs, including precipitable water vapour, surface spectral albedo, total column ozone, and model atmospheres varying month by month from ERA-5. The SBDART model then simulates both with and without aerosol fluxes thus computing net TOA forcing associated to BC.

The negative regional values reported in our results should therefore not be directly compared with the low positive global mean BC forcing values cited in the Introduction. Those literature values represent globally averaged BC forcing estimates. In contrast, our values are clear-sky, high-resolution, regional instantaneous TOA direct radiative effects over two heavily polluted urban agglomerations, computed for observation-constrained grid-days. In addition, our quantity represents the net TOA effect of BC-containing core-shell particles, where absorption by the BC core and scattering by the coating/column extinction act simultaneously. Under conditions of strong coating and high column extinction, scattering can dominate the TOA balance and yield negative TOA forcing, even while BC absorption contributes to atmospheric heating. This absorption-scattering competition is central to the regional behaviour discussed in the manuscript. Yet at the same time, the variability between the urban sites is based on real differences, since Xuzhou is controlled much more by secondary aerosol growth, while Dhaka is controlled much more by primary emissions as explained in Tiwari et al., 2025.

Line 112: Can this framework be expanded to other regions with AERONET stations, or are there any other special requirements?

Yes, the framework can in principle be expanded to other regions with AERONET, SONET, or equivalent sun-sky photometer stations. The framework requires a set of overlapping observational cosntraints and ancillary inputs. The key requirement is the availability of overlapping multi-platform constraints needed to retrieve BC-specific microphysics and column loading in a physically consistent way.

Specifically, this study wanted to include a broad spectrum covering UV-VIS-NIR, thus, the framework requires quality-controlled multi-waveband SSA from AERONET, SONET, or an equivalent sun-sky photometer network; satellite UV-SSA or absorption-related constraints; multi-waveband total AOD to impose column-feasibility filtering. Other anciallary inputs will strengthen the radiative transfer simulation.

The broader transferability of this deriving BC size and mixing state within a observationally cosntrained framework philosophy is supported by recent top-down BC studies. For example, Liu et al. (2024a) used OMI and AERONET observations with an inverse Mie framework to estimate BC mass and number column density on a day-by-day and grid-by-grid basis over South, Southeast, and East Asia. Similarly, Liu et al. (2024b) applied remotely sensed SSA as constraint from MISR satellite along with SONET to derive and diagnose changes in BC mass, number, size, and mixing state over Western China. In both cases RTM simulations were not carried out but size and mixing state of BC coated with non-absorbing shell were derived using obsevrational constraint using SSA information from OMI, MISR, AERONET and SONET in tandem. More recently, Liu et al. (2026) demonstrated that a multi-angle, multi-band satellite and Mie-scattering framework can be scaled globally to retrieve BC column concentration and microphysical information.

These studies support the transferability of the core retrieval concept, while the present study further extends it by adding a multi-waveband total-AOD feasibility constraint and coupling the constrained BC optical properties with SBDART for clear-sky BCTOA DRF estimation.

Line 210-220: Reference to your earlier work is missing here. Abbreviations MBE and MAE need to be defined. A brief note on the variables used to predict BCTOA, type of random forest model used along with the hyperparameters would be useful here.

Thank you for this helpful suggestion. We have now more clearly defined the predictor variables, statistical metrics, Random Forest configuration, and connection to the earlier COSMO-based retrieval work. We have revised Section 2.2 accordingly.

The predictors used to estimate BCTOA are the COSMO-derived and RTM-relevant variables: BCAOD550, aerosol column number density (N_c), aerosol column mass density (M_c), BC core size, and mixing state (defined as the ratio of BC core size to total particle size). These predictors are derived from the earlier observation-constrained COSMO framework described in in section 2.1.

We also now define the performance metrics at first use: mean bias error (MBE), mean absolute error (MAE), root mean square error (RMSE), and coefficient of determination (R^2). In addition, we have specified that the ML model is a Random Forest Regressor. The hyperparameters used were: n_estimators=100, max_depth=10, min_samples_split=5, min_samples_leaf=3, and max_features='sqrt'.

These settings were selected as a regularized configuration to balance predictive accuracy and generalization. Specifically, the number of trees provides a stable ensemble estimate, while the maximum tree depth and minimum split/leaf sizes limit overly deep trees and reduce overfitting. The use of 'sqrt' feature sampling decorrelates individual trees and improves ensemble robustness. The suitability of this configuration is supported by the close agreement between training and independent test performance, near-zero MBE, high R^2, and the 5-fold cross-validation results reported in the Supplement Figure S1. The manuscript has been revised to include these details.

Revised manuscript text:

"Specifically, we used a Random Forest Regressor to predict COSMO-RTM derived BCTOA from the COSMO-derived predictor variables. The predictors were BCAOD550, aerosol column number density (N_C), aerosol column mass density (M_C), BC core size, and mixing state (defined as the ratio of BC core size to total particle size). These variables are derived from the observation-constrained COSMO retrieval framework described in Section 2.1. For each region's RTM output BC TOA is subjected to a 70-30 train-test split, with 70% of the data used to train the model and 30% withheld as an independent test set. This approach allowed the model to learn relationships between predictors and BC TOA while ensuring a robust evaluation on unseen data. The Random Forest hyperparameters were set as follows: n_estimators=100, max_depth=10, min_samples_split=5, min_samples_leaf=3, and max_features='sqrt'. These regularized settings were used to provide a stable ensemble prediction while limiting overfitting through restricted tree depth, minimum node sizes, and randomized feature selection.

The statistical metrics (coefficient of determination (R^2), mean bias error (MBE), mean absolute error (MAE) and root mean square error (RMSE)) for both the training and test data are presented, along with the corresponding predicted vs. actual plots for each set along with their statistics and error metrics provided in Supplement Figure S1 and Supplement Table S1 respectively."

Figure 3: Bottom panels are not correctly labelled. Also, the font size is too small for the last two panels in bottom row and should be increased.

Thank you for this helpful comment. We have revised Figure 3 to correct the bottom-panel labels and improve figure readability. The font sizes of the subplot titles, axis labels, tick labels, and legends have been increased throughout, with particular attention to the bottom-row panels.

We have also reorganized the bottom panels for clarity. The former small 2D core-shell KDE panels, previously shown as panels h and i, have been removed from the main figure, enlarged, and combined into a separate supplementary figure as Supplement Fig. S3. The revised Figure 3 now focuses on the one-dimensional probability density distributions of the key BC-related parameters, including the polluted-condition core-to-shell ratio, polluted-condition BC core size, and the $BCAOD_{550}$ distribution under small-core conditions.

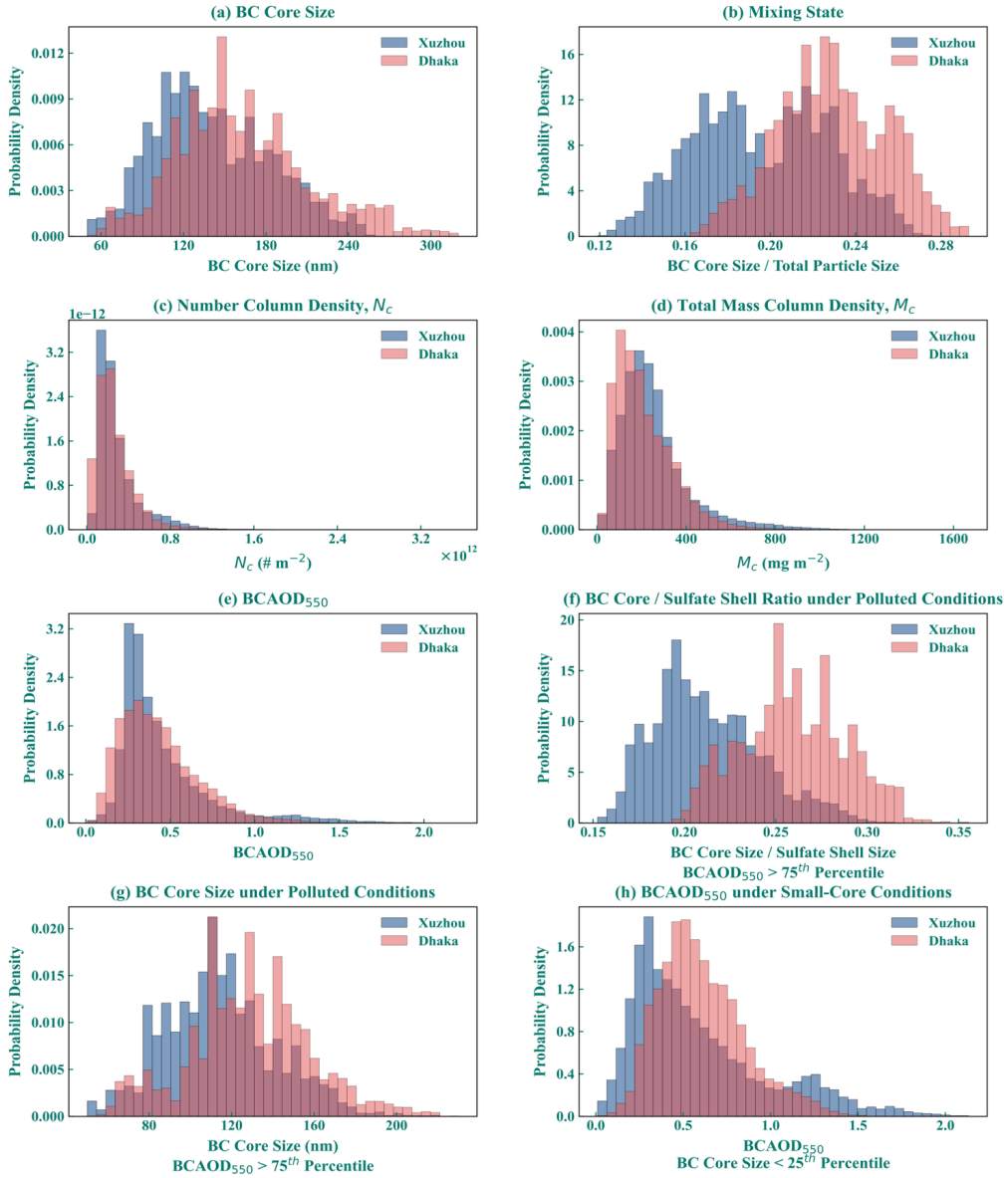

Figure 3: Probability density distributions of key predictors for aerosol radiative forcing analysis in Xuzhou and Dhaka: a.) Black Carbon (BC) core size, b.) Mixing state (ratio of BC size to total size), c.) Number column density (N_c), d.) Total mass column density (M_c), and e.) BCAOD at 550 nm, f.) BC core to Sulfate shell size ratio ($BCAOD_{550}$>75th percentile), g.) BC core size for polluted

condition ($BCAOD_{550}$>75th percentile), h.) $BCAOD_{550}$ distribution (BC core size < 25th Percentile or under barely coated conditions)

Supplement Figure S3.

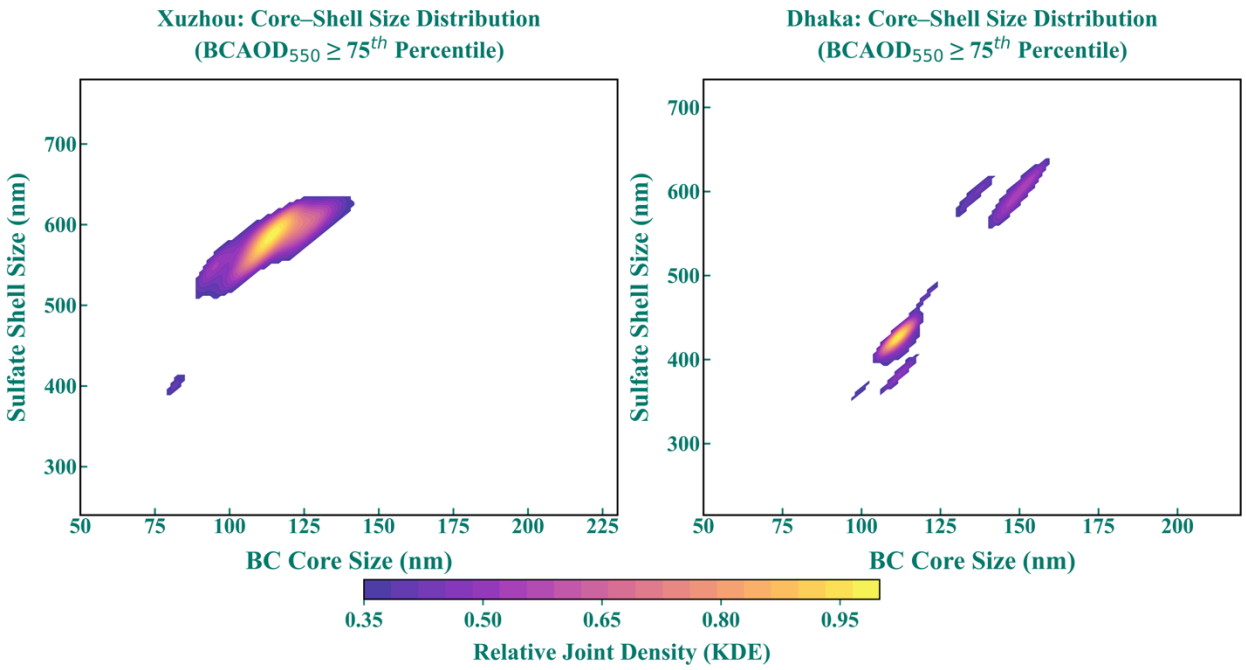

Supplement Figure S3. Dominant BC core-sulfate shell size distributions under polluted conditions ($BCAOD_{550}$ >75th percentile in Xuzhou and Dhaka. Color shading shows the relative joint KDE density normalized by the regional maximum, indicating the most frequent core–shell microphysical states during high-loading conditions.

Lines 280-335: While the values of the different BC-related parameters are taken from Figure 3, it would improve clarity if the corresponding panels (a–i) are explicitly referenced when these parameters are discussed.

In addition, we have revised the corresponding text in Lines 280–335 to explicitly reference the relevant Figure 3 panels when each parameter is discussed. The general BC microphysical and loading distributions are now linked to Fig. 3 (a-e), the polluted-condition core-to-shell ratio and BC core size distributions are linked to Fig. 3 (f,g), and the small-core BCAOD550 distribution is linked to Fig. 3 (h).

Section 3.2: The rationale for comparing different statistical models for predicting BCTOA is not stated in the manuscript. If the authors wanted to show the benefit of using a random-forest model compared to multi-linear regression or linear regression, they could just state the additional information in the supplementary or appendix. Adding a separate section for this

comparison seems unnecessary and I suggest moving this section to supplementary and briefly stating the benefit of using ML-based model in the main text.

We thank the reviewer for highlighting this, and we take this as an opportunity to better articulate the scientific value of this comparison, which goes beyond a methodological benchmarking exercise, since we do agree with the comment that from a purely methodological perspective it makes sense to move this to the appendix.

The rationale for comparing the three surrogate models is established in Section 2.2, where we note that the atmospheric science community still commonly adopts a linear radiative efficiency approach by assuming TOA forcing scales linearly with AOD - a widespread simplification, that "**overlooks non-linear modulations in TOA forcing caused by microphysical variability, column number loading, and their role in both absorption and extinction efficiency**." The three models are designed precisely to test this hierarchy of complexity based on the current trends following the atmospheric radiative forcing community: the linear model mimicking community practice, the MLR model expanding to additional predictors while retaining linearity, and the random forest model capturing nonlinear interactions. We acknowledge, however, that this connection between Section 2.2 and Section 3.2 could have been stated more explicitly, and we add a brief bridging paragraph at the opening of Section 3.2 to make this clearer.

Beyond model comparison, Section 3.2 serves three interconnected scientific purposes that we feel warrant its retention in the main text:

First, it quantifies the real-world cost of the linear approximation across diverse pollution and microphysical regimes. The finding that the linear model fails entirely under barely-coated BC conditions in Xuzhou (Adj. R^2 = -0.20) and degrades severely for very large BC cores (MAPE = 38.6%) is a physically meaningful result that directly supports the paper's central argument that simplified BC forcing parameterizations are inadequate.

Second, it reveals the transition-regime problem, where models including ML exhibit reduced variance explanation despite low absolute errors in mid-range TOA categories. This bias-variance trade-off is not a routine modeling artifact - it reflects the complex, competing absorption-scattering dynamics that govern the crossover between cooling and warming regimes, which directly motivates the SHAP analysis presented in Section 3.3. Relocating Section 3.2 to supplementary material would therefore sever this narrative connection.

Third, the regime-stratified performance analysis across coating thickness and BC core size categories provides physical insight into which atmospheric conditions pose the greatest challenge for simplified approaches, reinforcing the paper's conclusion that no universal BC forcing parameterization is currently feasible.

We therefore propose retaining Section 3.2 in the main text, with the addition of a bridging paragraph that more explicitly connects the motivation established in Section 2.2 to the results that follow. We are happy to further revise if the reviewer feels additional changes are needed.

In the revised manuscript, we have added the following sentences at the opening of Section 3.2 to better articulate the scientific rationale for this comparison:

"*As outlined in Section 2.2, the three surrogate models span a deliberate complexity gradient, from AOD-only linear scaling, to multivariate parametric regression, and ultimately nonlinear ensemble learning, with each model tier designed to probe a distinct aspect of BC-radiation interaction. Their performance is assessed both in aggregate and across distinct pollution, coating, and size regimes, where the physical drivers of BC TOA forcing are expected to differ most.*"

Section 3.2: please refer to specific panels in Figure 4 appropriately while discussing them in the text.

We thank the reviewer for this observation. Specific panel references have been added in Section 3.2, with scatter density comparisons referenced as Figures 4a-c for Xuzhou and Figures 4d–f for Dhaka. Percentile-based distributional comparisons are now referenced to Supplementary Figure S4, which shows the PDF plots relocated from the original Figure 4.

Figures 4 and 6: Axis labels are hard to read. Please increase their font size.

We thank the reviewer for this observation. In the revised manuscript, Figure 4 has been reorganized to address concerns raised by regarding figure crowding. Specifically, the PDF comparison plots between the surrogate models and SBDART BCTOA have been relocated to Supplementary Figure S4, allowing Figure 4 to focus solely on the scatter density plots for Xuzhou (Figures 4a-c) and Dhaka (Figures 4d-f). This reorganization also allowed us to increase the font sizes of axis labels, tick marks, and legend text throughout Figure 4 to improve readability.

The revised Figure 4 is shown below for convinience:

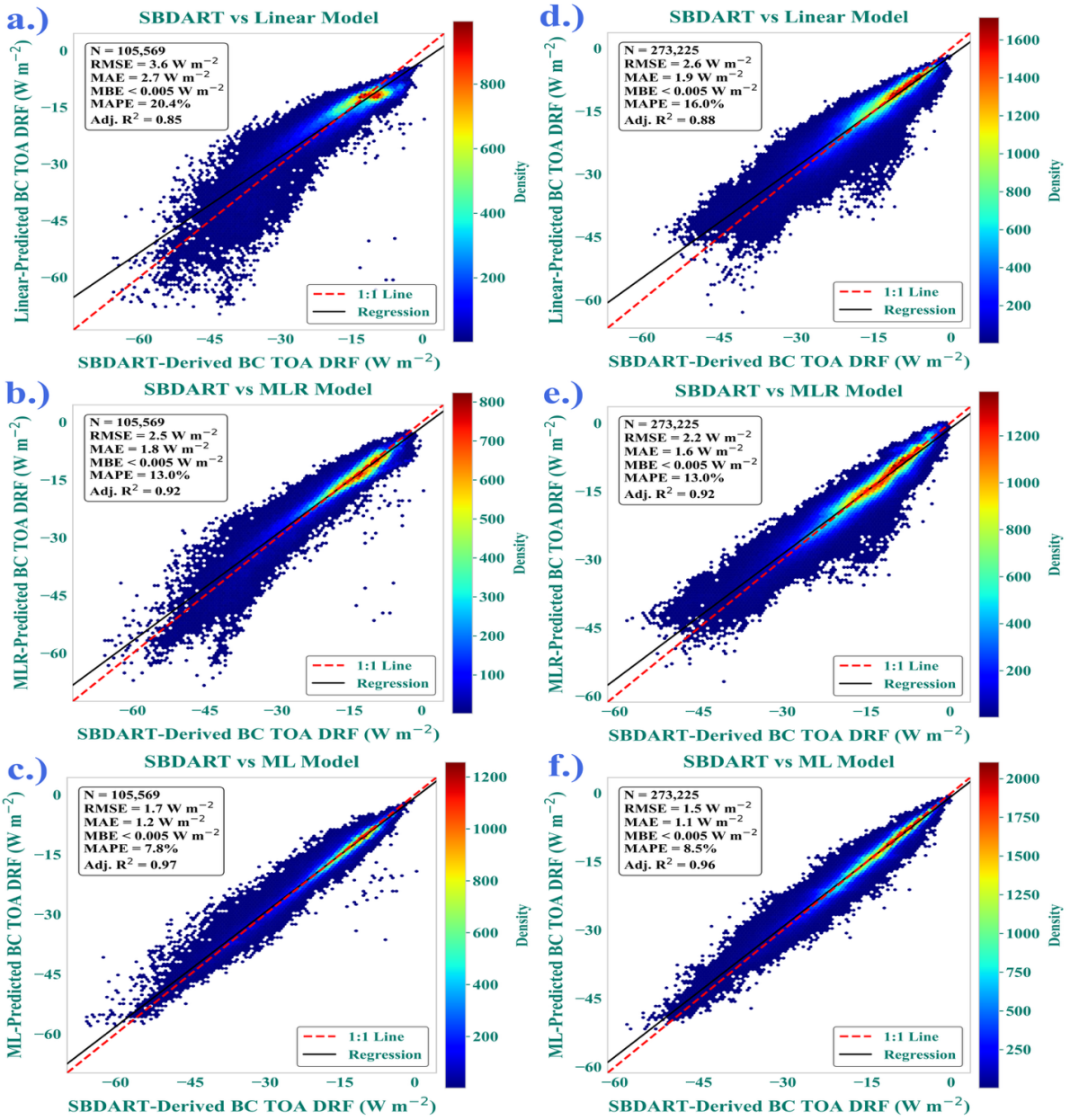

Figure 4: Comparison of BCTOA predictions from various models (Linear, MLR, and ML) with SBDART TOA for Xuzhou (a-c) and Dhaka (d-f). The scatter plots (top row) display the relationship between model predictions and SBDART values, with color maps indicating the density of data points.

The PDF plots have now been replotted and moved in to the Supplement Figure S3:

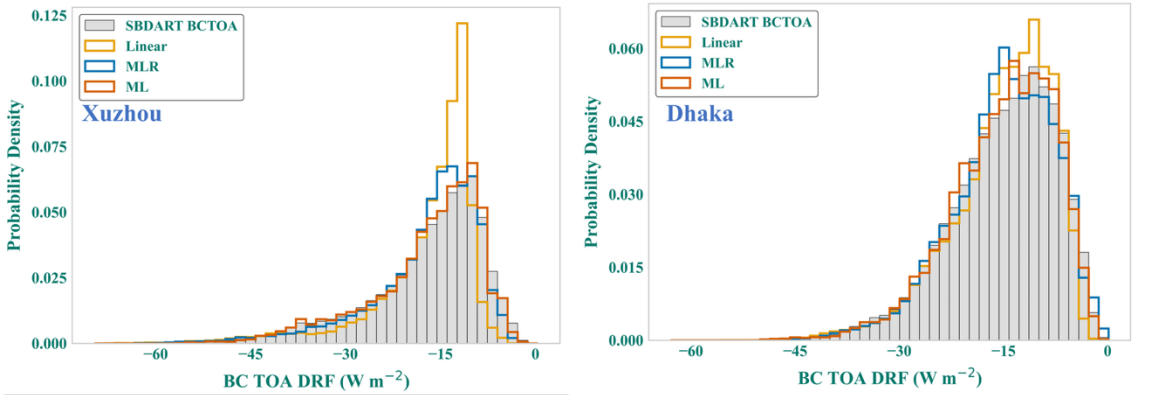

Percentile	SBDART	Linear	MLR	ML
1st	-45.4	-49.0	-47.9	-43.9
99th	-4.1	-7.2	-5.1	-4.5

Percentile	SBDART	Linear	MLR	ML
1st	-37.1	-37.6	-36.5	-36.5
99th	-2.8	-4.4	-2.2	-3.1

Figure S4: Probability density functions (PDFs) of BCTOA values from SBDART and the three surrogate models (Linear, MLR, and ML) for Xuzhou (left) and Dhaka (right). Tabulated percentile values at the 1st and 99th percentiles are provided below each panel to compare the distributional extremes.

Similarly, for Figure 6 we have revised and re-organized the plot for clarity as shown below:

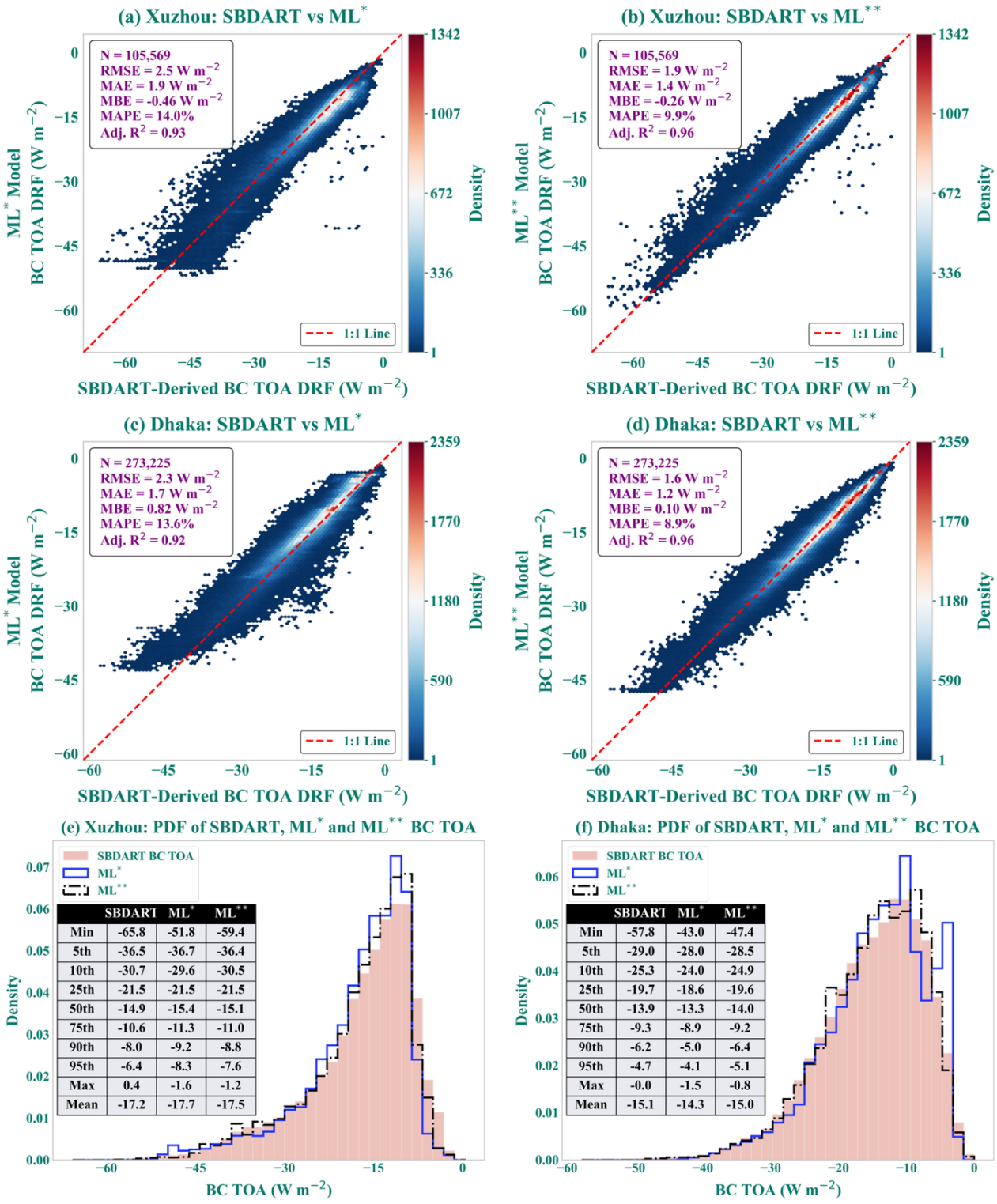

Figure 6: Comparison of SBDART-derived BCTOA forcing with cross-regional (ML*) and combined (ML) ensemble learning models for Xuzhou (a-b) and Dhaka (c-d). PDF comparisons**

between SBDART BCTOA and ML-predicted BCTOA, with statistical summaries of BCTOA distributions at different percentiles (e-f).

Line 392: By "environmental" do you mean different source regions?

We thank the reviewer for this observation. Then intention was to compare performance of models across different in-situ microphysical conditions of coating thickness and core size, attempting to account for atmospheric aging, oxidant availability, and emission characteristics. We acknowledge the term is may seem out of place or ambiguous here since Table 1 strictly stratifies specifically by microphysical regimes. We have revised the sentence to:

"To assess model performance under different microphysical conditions, performance metrics are compared across distinct mixing state and BC core size regimes and tabulated in Table 1."

Lines 455-465: Please correct repeated information.

We thank the reviewer for this observation. The repeated reference to *Tiwari et al., (2023)* and the reiteration of the scattering-absorption argument in Lines 455-465 have been removed and consolidated into a single concise statement in the revised manuscript. The revised manuscript now reads:

"*This microphysics-driven TOA sign variability, previously demonstrated by Tiwari et al., (2023), likely arises from non-linear changes in absorption, scattering and scattering angle that occur simultaneously with small changes in the mixing ratio and core size in tandem. While such interactions and sensitivity are often high AOD contributing to more negative TOA forcing is consistent with the total attenuation under the conditions where scattering enhancement is larger than the absorption enhancement.*"

Line 536: Please include the number of years of data that was used in generating the "regional climatology" shown in Figure 7?

The spatial maps in Figure 7 represent pixel-by-pixel weighted averages computed across all available clear-sky observation days spanning April 2018 to April 2022. Accordingly we have revised the caption of Figure 7.

Figures 7 and 8: What geographical radius was used for estimating BC TOA DRF around each AERONET station? How were this radius chosen?

We thank the reviewer for this question. The spatial maps in Figures 7 and 8 were generated over a 150 km radius Haversine circle centered on the AERONET station in each region (Xuzhou_CUMT for Xuzhou; Dhaka_University for Dhaka).

The 150 km radius was chosen based on several considerations. First, under typical strong wind conditions of ~5 m/s, air parcels would require many hours to traverse 150 km, meaning absorbing aerosol properties observed at the AERONET station on a given day remain physically

representative within this distance. Second, existing literature supports AERONET's spatial representativeness extending up to 200–400 km under stable aerosol conditions (Fu et al., 2018; Mishra et al., 2016), making 150 km a conservative and defensible choice. Third, this radius avoids the overly broad assumptions of a 2° × 2° grid representativeness that may dilute regional detail, while also avoiding finer scales that risk losing broader spatial coherence essential for regional characterization (Wang et al., 2018; Schutgens, 2020).

Critically, the 150 km radius is used only to define the spatial domain over which BC microphysical type - constrained through multi-waveband SSA consistency is assumed representative. Column loading quantities such as mass and number density are derived independently for each valid pixel based on actual satellite observations, with no spatial homogeneity assumption applied to aerosol abundance.

In summary, the 150 km radius represents a balanced and physically motivated choice that preserves both spatial relevance and regional coherence. It is conservative enough to maintain optical consistency across retained pixels while being broad enough to capture the regional aerosol environment characteristic of each urban agglomeration.

We acknowledge that as denser observational networks and higher resolution geostationary data become available, these spatial boundaries can be further refined to better capture fine-scale aerosol heterogeneity within and around these regions.

References:

Biswas, J., Pathak, B., Patadia, F., Bhuyan, P. K., Gogoi, M. M., & Babu, S. S. (2017). Satellite-retrieved direct radiative forcing of aerosols over North-East India and adjoining areas: climatology and impact assessment. *International Journal of Climatology*, *37*(13), 4756. https://doi.org/10.1002/joc.5325

Christopher, S. A., & Zhang, J. (2002). Shortwave Aerosol Radiative Forcing from MODIS and CERES observations over the oceans. *Geophysical Research Letters*, *29*(18). https://doi.org/10.1029/2002gl014803

Fu, D., Xia, X., Wang, J., Zhang, X., Li, X., & Liu, J. (2018). Synergy of AERONET and MODIS AOD products in the estimation of PM2.5 concentrations in Beijing. *Scientific Reports*, *8*(1), 10174. https://doi.org/10.1038/s41598-018-28535-2

He, L., Wang, L., Lin, A., Zhang, M., Bilal, M., & Tao, M. (2017). Aerosol Optical Properties and Associated Direct Radiative Forcing over the Yangtze River Basin during 2001–2015. *Remote Sensing*, *9*(7), 746. https://doi.org/10.3390/rs9070746

Liu, J., Cohen, J. B., Tiwari, P., Liu, Z., Yim, S. H., Gupta, P., & Qin, K. (2024a). New top-down estimation of daily mass and number column density of black carbon driven by OMI and AERONET observations. *Remote Sensing of Environment*, *315*, 114436. https://doi.org/10.1016/j.rse.2024.114436

Liu, Z., Cohen, J. B., Tiwari, P., Guan, L., Wang, S., Li, Z., & Qin, K. (2026). A global black carbon dataset of column concentration and microphysical information derived from MISR multi-band observations and Mie scattering simulations. *Earth System Science Data*, *18*(1), 507–533. https://doi.org/10.5194/essd-18-507-2026

Liu, Z., Cohen, J. B., Wang, S., Wang, X., Tiwari, P., & Qin, K. (2024b). Remotely sensed BC columns over rapidly changing Western China show significant decreases in mass and inconsistent changes in number, size, and mixing properties due to policy actions. *Npj Climate and Atmospheric Science*, *7*(1). https://doi.org/10.1038/s41612-024-00663-9

Mishra, A. K., Rudich, Y., & Koren, I. (2016). Spatial boundaries of Aerosol Robotic Network observations over the Mediterranean basin. *Geophysical Research Letters*, *43*(5), 2259–2266. https://doi.org/10.1002/2015gl067630
Schutgens, N. a. J. (2020). Site representativity of AERONET and GAW remotely sensed aerosol optical thickness and absorbing aerosol optical thickness observations. *Atmospheric Chemistry and Physics*, *20*(12), 7473–7488. https://doi.org/10.5194/acp-20-7473-2020

Sundström, A., Arola, A., Kolmonen, P., Xue, Y., De Leeuw, G., & Kulmala, M. (2015). On the use of a satellite remote-sensing-based approach for determining aerosol direct radiative effect over land: a case study over China. *Atmospheric Chemistry and Physics*, *15*(1), 505–518. https://doi.org/10.5194/acp-15-505-2015

Tiwari, P., Cohen, J. B., Lu, L., Wang, S., Li, X., Guan, L., Liu, Z., Li, Z., & Qin, K. (2025). Multi-platform observations and constraints reveal overlooked urban sources of black carbon in Xuzhou and Dhaka. *Communications Earth & Environment*, *6*(1). https://doi.org/10.1038/s43247-025-02012-x

Wang, R., Andrews, E., Balkanski, Y., Boucher, O., Myhre, G., Samset, B. H., Schulz, M., Schuster, G. L., Valari, M., & Tao, S. (2018). Spatial representativeness error in the Ground-Level observation networks for black carbon radiation absorption. *Geophysical Research Letters*, *45*(4), 2106–2114. https://doi.org/10.1002/2017gl076817

Response to Reviewer 2 Queries/Comments

Citation: https://doi.org/10.5194/egusphere-2026-363-RC2

Dear Editor and Reviewer,

We appreciate you taking the time to provide us with all of your insightful and valuable comments and recommendations. All of them have been carefully considered, and we have made a concerted effort to answer them all in detail. Your unaltered original remarks are written in **grey** in this response, while our responses are written in **blue**. Certain key highlights in some of the responses have been emphasized using **bold text**.

General Comments:

This manuscript presents a physics-informed machine learning (ML) framework to estimate clear-sky black carbon (BC) top-of-atmosphere (TOA) direct radiative forcing by combining observationally constrained microphysical retrievals (via a core-shell Mie framework) with radiative transfer modeling (SBDART), and subsequently training surrogate models for rapid prediction. The approach is applied to two contrasting urban regions (Xuzhou and Dhaka), and the authors further interpret controlling factors using SHAP analysis. While the study addresses an important issue, i.e., BC forcing uncertainty, it currently has several conceptual and methodological limitations that limit the robustness and general applicability of the conclusions, as detailed in my specific comments below.

We thank the reviewer for the careful and constructive evaluation of our manuscript. We appreciate the detailed comments and believe they provide us with an opportunity to strengthen the scientific clarity, results and conclusions of this work. We note that some of the concerns raised are consistent with limitations already acknowledged in the manuscript, and we welcome the opportunity to elaborate on the physical reasoning and observational constraints that motivated our methodological choices. We do believe that our choices actually are robust and reasonably applicable, and welcome this opportunity to demonstrate in more depth. In response, we performed several new analyses and revisions:

- **Mixing-state assumption:** We added observational support for the spherical-particle assumption using AERONET depolarization ratios and evaluated the physical consistency of the retrieved BC microphysical properties. We have taken the time to perform a targeted external-mixing endmember sensitivity test and clarified why partial internal mixing, homogeneous internal mixing, and fractal aggregate treatments require separate optical models and additional morphology parameters that are not constrained by existing observation sets.

- **Vertical aerosol distribution:** We clarified the aerosol vertical-profile assumption used in SBDART and added discussion of the companion CALIPSO-constrained sensitivity analysis, which evaluates the impact of redistributing aerosol from the baseline near-surface-dominant profile to elevated aerosol layers.
- **COSMO-RTM forcing target:** We added an AERONET-based forcing-efficiency consistency assessment over Dhaka to evaluate the physical coherence of the COSMO-RTM BC TOA DRF target. This includes temporal consistency analysis, regime-dependent analysis and a relative-scaling diagnostic comparing COSMO-RTM BC-only TOA forcing efficiency with AERONET total-aerosol TOA forcing efficiency.
- **Model transferability:** We have performed additional analysis and evaluation over two new regions: Delhi, India representing a mixed urban-agricultural-burning environment during the post-monsoon period, and Mongu, Zambia, representing a remote dry-season savanna biomass-burning regime. We first conducted zero-shot transferability tests using the original Xuzhou-Dhaka trained model (over China and Bangladesh) over Delhi, India and Mongu, Zambia, conducted feature-space diagnostics, and improved our combined ML surrogate.
- SHAP result statement have been revised according to the suggestion of the reviewer

We believe that we have addressed all comments carefully and responded appropriately in the revised version. Please see below for detailed point-by-point responses.

Major Comments:

1. The COSMO model assumes the core-shell model for internal mixing. This will largely enhance the absorption of BC. But the actual mixing states may be different. I suggest the authors perform additional sensitivity experiments to test the effect of other mixing states, such as external mixing, partial internal mixing, uniform internal mixing, fractal aggregates, etc.

We appreciate the reviewer's concern regarding the structural assumption of core-shell internal mixing. We wish to emphasize that this limitation was explicitly acknowledged in the Discussion of the original manuscript: "*The use of a core-shell representation with a non-absorbing sulfate proxy reflects a deliberate optical constraint. Although urban aerosols arise from diverse emission sources, extensive field evidence across urban, industrial, and biomass-burning regions in East and South Asia indicates that BC is frequently internally mixed and coated by optically similar inorganic and organic material (Kompalli et al., 2021; Peng et al., 2016; Sun et al., 2024; Zamora et al., 2019), supporting the physical relevance of this assumption. However, particles with irregular shapes, including fractal aggregates and agglomerated structures are known to occur prominently in freshly emitted BC, and are not explicitly addressed in this study. Future extensions could reconcile this limitation through hybrid frameworks that couple fractal or irregular morphologies at emission with spherical coated particles at advanced aging stages.*"

Thus using core-shell was a deliberate scope boundary grounded in the study's central objective:

- **to develop multi-platform, multi-waveband observation-constrained BC microphysics, column, optical, and radiative properties within a core-shell framework.**
- **to use the observationally constrained BC TOA DRF to be predicted using a surrogate machine-learning emulator, and to examine how predictors influence TOA variability.**

The study was therefore not designed to conduct an exhaustive aerosol-morphology sensitivity study, in part because the observations currently available to the community do not yet support such a study's practical application, and because existing morphology-resolved frameworks face recognised challenges in simultaneously matching size distributions and multi-wavelength optical observations. However, such an extension represents an interesting future objective to explore, which will further help constrain the structural uncertainties in BC radiative forcing across diverse emission and aging regimes.

Nevertheless, the COSMO multi-waveband dual constraint approach advances the current community practice. For instance, CMIP6 models, OPAC-derived cliamtologies or MERRA-2 and CAMS reanalysis products typically prescribe BC size distribution, fix mixing state to globally uniform parameters, only use one waveband (or color) for their analysis, and/or use simple external mixing scenarios. These prescriptions are not dynamically constrained by observations at the pixel level. The COSMO framework, despite not being fully morphologically representative, retrieves BC core size, mixing state, column loading from multi-waveband observations on a pixel by pixel and day-by-day basis. **We therefore believe, that our inversion approach is a set of deliberate assumptions allowing for a tractable community advance, moving from prescribed, scenario-based microphysics toward observationally constrained, dynamically variable BC optical properties and radiative effects.**

Observational support for the spherical core-shell framework and retrieved microphysical consistency.

First, we would like to provide observational evidence supporting the spherical Mie assumption and the physical realism of our retrieved microphysical properties from the COSMO framework.

AERONET depolarization ratio (δ) at 440 nm provides observational support that the column-aerosol populations at our study sites are dominated by spherical or near-spherical particles (Figure 1). However, depolarization does not directly diagnose the internal BC coating structure; therefore, we use it as support for the spherical-scattering assumption, not as independent proof of a core-shell morphology. At Dhaka δ (min/median/mean/max) were 0.002/0.03/0.04/0.19 and 85.8% of retrievals exhibit $\delta < 0.10$ (more spherical), with only 1.3% moderately non-spherical ($\delta = 0.15$-0.20) and zero highly non-spherical particles ($\delta > 0.20$). At Delhi during the post-monsoon crop-residue burning period, 91.5% are spherical like with 8.5% slightly non-spherical and none highly non-spherical. Delhi δ (min/median/mean/max) were 0.003/0.03/0.04/0.15. At Mongu δ (min/median/mean/max) were 0.002/0.004/0.004/0.03 during the savanna-fire season, here 100% of retrievals were observed to be more spherical like ($\delta < 0.10$) with zero non-spherical fraction. The low depolarization ratios support the use of a spherical Mie framework for the column aerosol population.

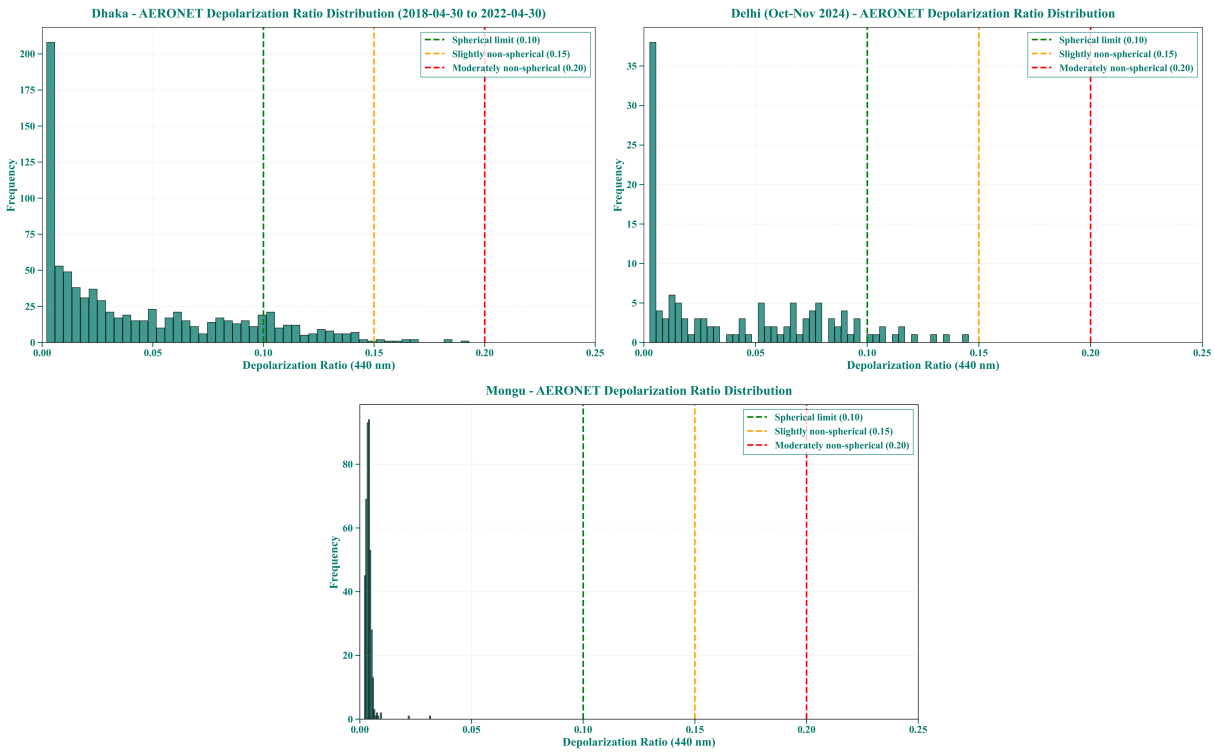

Figure 1: Depolarization ratio distributions at 440 nm across all sites. Dashed lines denote spherical (0.10), slightly non-spherical (0.15), and moderately non-spherical (0.20) thresholds.

Furthermore, the retrieved microphysical properties generated from this framework are broadly consistent with independent observations and inverse-modeling studies. To start with, the ensemble-derived BC core size varies across aerosol regimes- (median ~ 140 nm in Xuzhou, median ~155 nm in Dhaka; median ~115nm in Delhi, and median ~103 nm in Mongu) - a range that aligns with the broad envelope of SP2-measured ambient BC cores. For example, Huang et al. (2012) reported rBC core mass-equivalent diameters peaking at ~210 nm (radius ~105 nm) in urban Shenzhen, another study by Huang et al. (2011) observed core sizes up to 220 nm over Kaiping China. Ahlberg et al. (2023) observed rBC core diameters extending to 200-300 nm (radius 100-150 nm) in European air influenced by long-range transport. Reddington et al. (2013) similarly reported SP2-detected BC cores spanning 90-400 nm across different aging stage and across different regions. Similarly, In-situ SP2 measurements of African biomass burning smoke consistently report BC core count median size in the range of ~100-200 nm, with values varying by transport age and fire type (Wu et al., 2021). In addition, satellite derived BC column number concentrations (N_c) further corroborate the physical realism of the retrieval. Z. Liu et al. (2024) reported N_c over Xi'an in the range 1.3×10^{10} to 5×10^{10} # m^{-2}, which falls within the lower extreme of our distributions, consistent with the fact that while Xi'an is polluted, it is generally less so than the other places considered in this work. J. Liu et al. (2024a), using a coarser-resolution OMI-AERONET inverse Mie approach, reported region-wide N_c values up to the order of 10^{13} # m^{-2}, with the upper end of our ranges overlapping their interquartile spread. All three studies share the same non-normal distribution characteristics. This provides cross-parameter confidence that the observation-constrained optical and microphysical properties are physically plausible.

Targeted External Mixing Sensitivity: A Quantitative Test of Observational Consistency

To directly address the reviewer's request for additional sensitivity experiments, we tested an external mixing assumption within the same Mie-based framework. We focused this sensitivity test on Delhi, India and Mongu, Zambia.

Under external mixing, the COSMO setup reduces to two independent homogeneous-sphere Mie calculations (one for BC and one for sulfate), both computed over the same size ranges as the core-shell retrieval (BC radius 50-500 nm; sulfate radius 10-800 nm). We applied the same day-by-day AERONET VIS-NIR SSA uncertainty bounds (440, 675, 870, and 1020 nm) that were used in the original core-shell retrieval. Before applying the full constraint pipeline (including TROPOMI UV at 388 nm and AOD upper bounds), we first evaluated whether external mixing could reproduce observed SSA within uncertainty bounds for the four AERONET wavebands in tandem. This is a deliberately generous test. The column-effective SSA under external mixing is calculated as an extinction-weighted average:

$$SSA_{external} = f_{BC} \times SSA_{BC} + f_{sul} \times SSA_{sul}$$

Where f_{BC} and f_{Sul} represent the fractional contributions of BC and sulfate to total column extinction respectively, with $f_{BC} + f_{sul} = 1$. Because this extinction fraction is not directly retrievable from column-integrated SSA observations alone, we tested five physically distinct and bracketing scenarios (S1 - S5). S1 as Pure BC (f_{BC} = 1.00); S2 as BC-dominated (f_{BC} = 0.75); S3 as equally externally mixed (f_{BC} = 0.5), S4 as sulfate-dominated (f_{BC} = 0.25), and S5 as pure sulfate (f_{BC} = 0.00). For each scenario and each observation day, the mixture SSA (SSAexternal) was computed across all combinations of BC core size (50-500 nm) and sulfate radius (10-800 nm) and evaluated against the observed AERONET SSA bounds at all four wavebands. Figure 2 presents the survival rate of externally mixed BC-sulfate size combinations against observed day-by-day AERONET SSA bounds at each of the VIS-NIR wavebands across different extinction fraction scenarios at Delhi and Mongu.

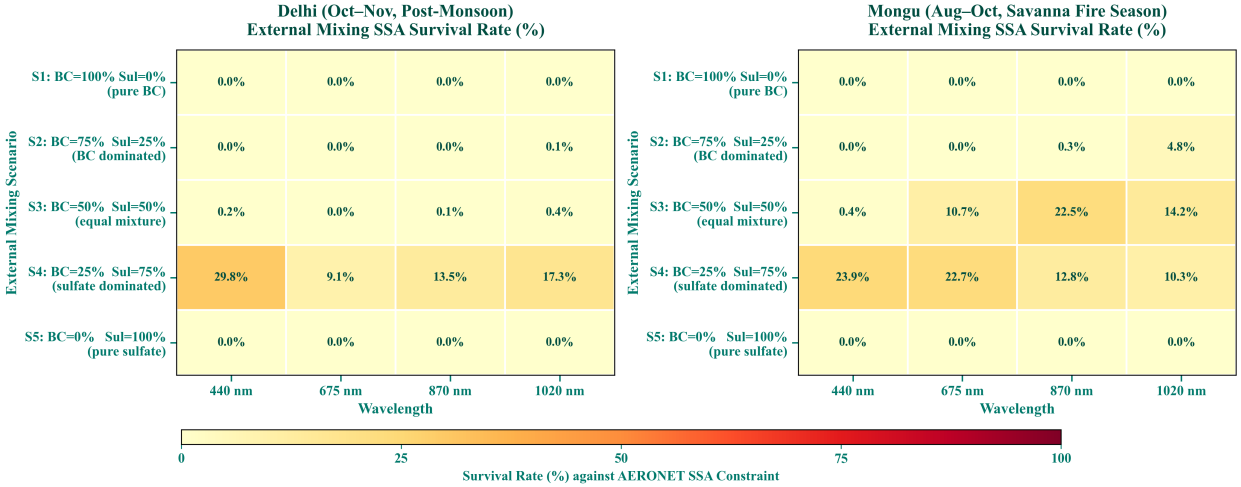

Figure 2: Survival rate (%) of externally mixed BC-sulfate solutions that satisfy the observed AERONET SSA uncertainty bounds at 440, 675, 870, and 1020 nm. Results are shown for five bracketing extinction fraction scenarios

Pure externally mixed BC (S1, f_{BC} = 1.00) achieves 0.0% survival at every waveband at both Delhi and Mongu as no BC size (from the external mixed pool), regardless of radius, produces SSA values consistent with observations. BC-dominated mixtures (S2, f_{BC} = 0.75) are similarly unable to satisfy the observational constraint, with survival rates of 0.0% at nearly all wavebands at Delhi and near-zero at Mongu (maximum 4.8% at 1020 nm only). The equal mixture scenario (S3, f_{BC} = 0.50) shows marginal and spectrally inconsistent survival - at Delhi, survival does not exceed 0.4% at any waveband, while at Mongu, survival reaches 22.5% at 870 nm but drops to 0.4% at 440 nm - meaning solutions that pass at one waveband systematically fail at others. Pure sulfate (S_5, f_{BC} = 0.00) also achieves 0.0% survival at both sites, confirming that the observed SSA spectral signature is not reproducible by sulfate alone either.

Meaningful survival is observed only in the sulfate-dominated scenario (S4, f_{BC} = 0.25, f_{SuI} = 0.75), where survival rates reach 29.8%, 9.1%, 13.5%, and 17.3% at 440, 675, 870, and 1020 nm respectively at Delhi, and 23.9%, 22.7%, 12.8%, and 10.3% at Mongu. Despite testing five bracketing scenarios, the analysis reveals that only S4 retains a non-negligible solution pool across all four wavebands at both sites, making it the only scenario for which cross-waveband consistency can even be meaningfully examined.

Examining the solutions for corss-waveband cosistency check for the S4 microphysical solution pool reveals two critical issues that further undermine the physical realism of external mixing in a multi-waveband observational constrained framework.

- First, the number of observation days yielding at least one valid solution is substantially reduced compared to the core-shell COSMO retrieval. While COSMO returned solutions satisfying the multi-wavelength observational constraints throughout the valid observation period, the external mixing S4 scenario yields valid solutions on only ~43% of the days - a loss of 56.5% of observation days over Delhi, and at Mongu - a loss of 74% of observation days. This indicates a substantial loss of observational coverage under the tested external-mixing scenarios.
- Second, the BC core sizes of the surviving cross-waveband consistent S4 solutions are substantially larger than typical SP2-reported BC core sizes and therefore difficult to interpret as physically representative. At Delhi, surviving solutions exhibit mean and median BC core radii of approximately 378nm and 390nm respectively, which is double the size of both SP2 observations and our core-shell solutions. At Mongu, mean and median radii are approximately 240 nm and 220 nm respectively. In the absence of a scattering-enhancing sulfate shell, the Mie filter is forced to select anomalously large BC sizes. For bare BC spheres, increasing the size initially increases absorption efficiency faster than scattering efficiency, depressing SSA. However, in the Mie regime (size parameter x ~ 1-5), scattering efficiency eventually grows non-negligibly while absorption efficiency saturates, allowing a modest increase in the SSA ratio toward its upper bound for pure BC (~0.4-0.5). The model exploits this weak size-dependent SSA increase to partially compensate for the missing coating-induced scattering enhancement. Yet even at these inflated sizes, the SSA of pure BC remains far below observed AERONET values, and the multi-wavelength constraint cannot be satisfied without the sulfate fraction contribution.

Therefore, the present Mie-based inverse framework and its core-shell treatment are not only as a geometric convenience, instead they provide an observationally tractable effective optical representation which is completely consistent with the cross-waveband SSA constraints, while still maintaining physically plausible BC core sizes, and preserving full temporal coverage.
Furthermore, the full constraint pipeline additionally requires SSA consistency at TROPOMI UV (388nm) and compliance with multi-waveband AOD upper bounds. These constriants are likely going to further reduce the already depleated S4 solution space and further compress viable observation days. **Since the surviving external-mixing solutions cover less than half of the observation days and require unrealistically large BC cores, a full DRF calculation based on these solutions would not provide a robust observation-constrained sensitivity test. We therefore did not pursue it further.**

Inherent observational barriers in extending the core-shell framework
We also clarify why testing partial internal mixing, uniform (homogeneous) internal mixing, or fractal aggregates is not a straightforward sensitivity extension within our framework, but rather requires fundamentally different physical models and observational constraints.

- The current 'Core-shell' Mie theory treats the particle as a concentric sphere with a distinct absorbing core and a non-absorbing shell; the retrieved "core radius" and "shell thickness" are the geometric degrees of freedom that are constrained by observed spectral SSA and AOD.
- Partial internal mixing would require assuming, a priori, a coating completeness fraction or a population-level external/internal mixing ratio that is not retrieved by any of the observation platforms used here (AERONET, satellite reflectance). Thus to still maintain, multi-waveband SSA constraint while our approach freely allows core and shell sizes to change adapting to partial mixing requires an arbitrary assumptions about the mixing fraction or coating completeness that are not observationally constrained.
- Uniform (homogeneous) internal mixing would require effective-medium approximations (e.g., Maxwell-Garnett or Bruggeman) that blend BC and non-BC material into a single volume with no distinct core-shell interface; this changes the optical cross-sections, phase functions, and absorption enhancement calculations entirely, and there is no observationally constrained parameter in our current platform that specifies the volume-mixing ratio of BC within the particle.
- Fractal aggregates would require discrete-dipole approximation (DDA) or T-matrix calculations to compute optical properties in solar spectrum with morphological parameters (fractal dimension, monomer number, orientation distribution) that rely on TEM, but the input morphology comes from post-sampling TEM which does not occur in any of the solar radiative bands available. For this reason, such data are not provided by column-integrated optical measurements and may not be fully consistent with observed in-situ conditions. AERONET and satellite data for this set of reasons offer no direct constraint on these properties to be adapted within our multi-waveband multi-optic constrained framework.

Without site-specific TEM-derived parameters at every retrieval location, incorporating these morphologies would **transform our observationally constrained inverse retrieval into a largely a priori forward modeling exercise with many free parameters, many of which are not capable of being observed in-situ based on present technology.**

Searching literature alternatives to check their adaptability with our inverse framework

We further examined whether recent unified mixing-state frameworks could be adapted to our pixel-by-pixel, observationally constrained inverse retrieval. Although several studies have attempted to bridge multiple mixing states parametrically, their implementation within our framework is not tractable. For example:

- Recent work by Wang et al. (2025) has demonstrated the radiative significance of resolving multi-mixing structures-including partial coatings, embedded fractions, and fractal aggregates-**using TEM-characterized morphologies coupled with discrete dipole approximation (DDA)** and global climate modeling. However, their approach relies on site-specific TEM data to prescribe mixing-state distributions and a DDA database **built from fixed parameters (e.g., fractal dimension of 1.86, fractal prefactor kg = 3.49, and monomer number N = 100)**. Extending our methodology to this level would require simultaneously constraining six additional parameters (monomer radius, fractal dimension, monomer number, coating volume fraction, embedded fraction, and fractal prefactor) - far beyond what can be uniquely constrained by AERONET-TROPOMI SSA and MAIAC AOD observations. Additionally, it would require us to limit the size of the distribution solution which we have obtained, and would hence be inconsistent with our findings as well as some additional works (Guan et al., 2026a,b; Tirpitz et al., 2026). Moreover, TEM-derived morphological parameters are not available at the high spatial-temporal resolution, over our study regions. We further note that Wang et al. (2025) found the previous modeling studies using core-shell model underestimates DRE relative to particle-resolved multi-mixing structures, attributing this to simpllified core-shell with limited variability in coating thickness at specific sizes. **This suggests that the impact of the core-shell assumption is not necessarily a simple high-bias effect, especially when core and shell sizes are allowed to vary under multi-wavelength observational constraints.**
- Similarly, Wang et al. (2023) developed a parametric framework that **bridges external, partial, and core-shell mixing through a single coating-thickness distribution parameter (k)**, demonstrating that a continuous range of mixing states can be represented without explicit morphology-resolved calculations. Their global implementation in CESM-CAM6 and WRF-Chem uses a **fixed BC core count median diameter of 70 nm with geometric standard deviation 1.8, and a uniform k = 0.014 translating to a fixed monodisperse coating thickness of 70 nm. While this represents a meaningful advance over conventional fixed core-shell assumptions in climate models.** To implement Wang et al. (2023) unified framework within our inverse retrieval, we would need to assume a fixed k value (abandoning pixel-by-pixel variability) or introduce an unconstrained degree of freedom that cannot be validated

against observations. This would transform our observation-constrained retrieval into again an a priori sensitivity study.

In summary, these alternative frameworks that have adapted multi-mixing state for BC address the forward problem of prescribing morphology and computing radiative effects. Whereas the present study addresses this as an inverse problem, retrieving effective microphysics from observations constraining the size, mixing state, and number in tandem across all available observations and simultaneously computing associated optical properties to feed into RTM model. The core-shell treatment was therefore selected as the most observationally tractable inverse model, with the understanding that the retrieved "core radius" and "shell thickness" represent effective optical parameters that absorb structural uncertainties rather than true geometric dimensions. **We therefore consider comprehensive testing of these alternative multi-mixing scenarios as a valuable future work when observations become available, rather than a minor sensitivity analysis within the current study.**

Concluding Remarks

- The core-shell treatment is not a full representation of ambient BC morphology, and we acknowledge this limitation explicitly.
- Partial, uniform, and fractal mixing assumptions are not tunable parameters within our framework; each requires a distinct aerosol-optics theory with its own radiative-transfer implementation, lookup tables, and observational constraints that are not presently available. Furthermore, some of these alternative assumptions impose more restrictive a priori constraints than the core-shell framework.
- The external-mixing sensitivity test shows that, under the tested bracketing scenarios, external mixing provides limited cross-waveband consistency, requires unrealistically large BC cores in the surviving cases, and discards nearly half of all observation days.

Finally, we thank the reviewer again for raising this concern, which has helped us present more clearly why the core-shell framework used herein represents a observationally tractable inverse model given current multi-platform constraints. **This study does not claim to solve BC morphology and compute the DRF. It estimates BC radiative forcing using an observation-constrained effective optical representation via core-shell.** Full morphology-resolved sensitivity requires extra unobserved state variables and therefore belongs to a separate forward-modelling uncertainty study. Future studies, as denser single-particle observational datasets become available, should prioritize developing multi-mixing frameworks that can be rigorously constrained at the pixel level to reduce structural uncertainties in BC TOA DRF estimates.

2. The vertical distribution of BC also significantly affects its radiative effects, but is not discussed in the analysis. The authors should explicitly discuss what vertical profiles were assumed in SBDART, whether BC is assumed to be well mixed or prescribed, etc. How this profile assumption may lead to uncertainties in BC forcing.

We thank the reviewer for raising this important point. We fully agree that the vertical distribution of aerosol; including BC - is a meaningful source of uncertainty in radiative forcing estimates, particularly at the BC TOA. We address this comment in three parts: **(1) clarification of the vertical profile assumption used in SBDART, (2) observational constraints from CALIPSO that justify the baseline assumption, and (3) a quantitative sensitivity analysis specifically focused on BC TOA DRF, which is the primary forcing metric reported in this study.**

In the SBDART radiative transfer calculations optical properties of BC is assumed to be distributed within the boundary layer using a profile with maximum concentration near the surface and exponential decay with altitude. This profile is prescribed through the ZBAER and DBAER parameters in SBDART, which define the vertical levels and the fractional aerosol loading at each level. We acknowledge that this assumption introduces uncertainty, as the actual vertical distribution of aerosol, particularly transported BC can deviate from a simple near-surface profile.

A detailed characterisation of aerosol vertical structure over both study regions is provided in the companion paper (Supplementary Section S3 of Tiwari et al. 2026 (http://dx.doi.org/10.2139/ssrn.6604914)), using CALIPSO Level-2 5-km aerosol profile data (CAL_LID_L2_05kmAPro, Version 5.00). The key findings relevant to this study are summarised below, as the SBDART radiative transfer framework is identical in both works:

Layer Classification:

For each valid CALIPSO profile over the study domains, the dominant aerosol layer was identified based on the peak attenuated backscatter signal. Using a fixed boundary layer threshold of 2.0 km, the CALIPSO analysis finds that **94.8% of profiles over Xuzhou** and **96.4% over Dhaka** exhibit dominant aerosol layers with base altitudes below this threshold, with median base altitudes of approximately 0.16 km and 0.10 km respectively. Free-tropospheric (FT) aerosol layers with base altitude ≥ 2.0 km accounts for only 5.2% and 3.6% of profiles respectively.

Column optical contribution:

The base-altitude classification alone does not quantify how much FT layers contribute to the column-integrated optical loading. To address this, the integrated backscatter ratio R = IB(0-2 km) / IB(0-5 km) was computed for each profile. The median R is **0.92 over Xuzhou** and **0.98 over Dhaka**, with 73.7% and 84.5% of profiles respectively exhibiting R ≥ 0.80 - meaning that in the vast majority of profiles, at least 80% of the total column backscatter originates from within the boundary layer. This demonstrates that even when elevated layers are present, the within boundary layer dominates the column optical loading.

Characteristics of elevated layers:

For the subset of profiles with FT aerosol, the median peak extinction altitude is approximately **3.6 km over Xuzhou** and **3.0 km over Dhaka**, placing the most radiatively active portion of transported layers in the lower free troposphere. These layers are vertically compact, with median thicknesses of **0.84 km** (IQR: 0.64-1.44 km) over Xuzhou and **1.02 km** (IQR: 0.60-1.62 km) over Dhaka, consistent with the structure of transported aerosol plumes rather than diffuse vertical mixing.

Together, these observations indicate that the boundary-layer-dominated vertical profile used in the SBDART baseline configuration is physically representative of BC aerosol conditions in both study regions across the vast majority of observation days.

Quantitative BC TOA DRF sensitivity analysis:

To directly bound the uncertainty introduced by the vertical profile assumption specifically for BC TOA DRF, the primary radiative forcing metric in this study we conducted a dedicated sensitivity experiment using the same SBDART framework.

The sensitivity analysis was restricted to the most radiatively extreme cases in each dataset, defined as pixel-level observations where BCAOD exceeds the 80th percentile and SSA falls below the 20th percentile threshold, with the condition satisfied at a minimum of two out of three wavelengths (388, 470, and 550 nm). This filtering yields **72 pixel observations over Xuzhou** and **506 pixel observations over Dhaka** - each a unique spatial location on highly polluted days, representing the upper-bound sensitivity scenario.

For each selected case, SBDART was run twice: **once under the baseline boundary-layer-dominated vertical profile, and once with the aerosol column redistributed into an elevated layer centered at the CALIPSO-derived median peak extinction altitude (3.6 km for Xuzhou; 3.0 km for Dhaka), with vertical extent equal to the characteristic CALIPSO-derived layer thickness (0.84 km for Xuzhou; 1.02 km for Dhaka). Column-integrated optical properties (AOD, SSA, asymmetry factor) were held consistent between the two configurations so that only the effect of vertical placement is evaluated.**

The resulting sensitivity from Figure 3 shows that the BC TOA DRF probability-density distributions from the baseline and elevated-layer simulations overlap almost entirely in both regions, indicating that vertical redistribution of the aerosol column does not substantially shift the modelled forcing distribution. This is quantitatively supported by the difference analysis. Absolute BC TOA DRF perturbations are small, with median values of approximately 0.2 W m^{-2} over Xuzhou and 0.1 W m^{-2} over Dhaka, and 95th percentile values remaining below 0.4 W m^{-2}. In relative terms, the median change is 0.9% over Xuzhou and 0.6% over Dhaka, with the 95th percentile reaching only 1.9% and 1.3% respectively. The Empirical Cumulative Distribution Function (ECDF) (bottom panel) reinforces this conclusion as the steep rise at low relative-change values confirms that the small sensitivity is not an artefact of a few outlier cases but is systematic across the entire high-loading subset, with nearly all cases falling below the 2% reference threshold.

Critically, this experiment was deliberately designed to represent an upper-bound scenario, restricted to the most strongly absorbing, highest-loading pixel observations in the record, where sensitivity to vertical redistribution is expected to be maximised. The corresponding sensitivity under more moderate or scattering-dominated conditions is expected to be smaller. The boundary-layer-dominated vertical profile assumption therefore introduces only modest uncertainty in the TOA BC DRF estimates reported in this study. With the radiative differences induced by the vertical redistribution currently smaller than the underlying observational uncertainty.

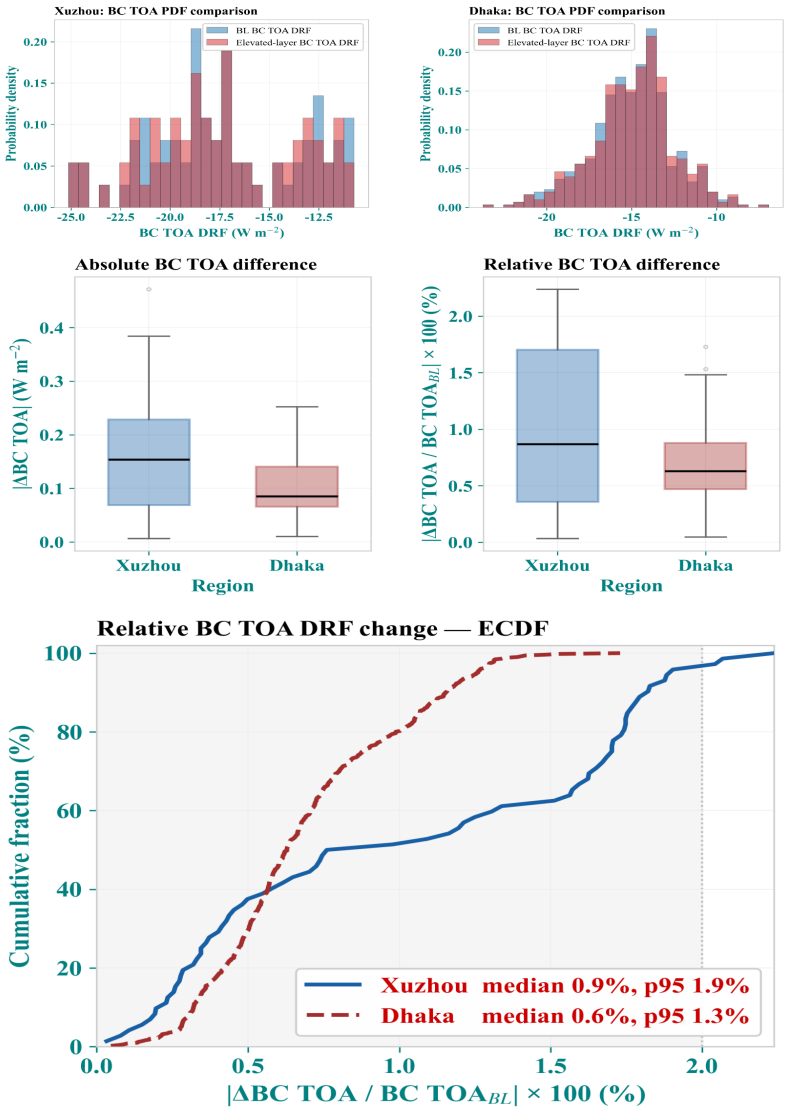

Figure 3: Sensitivity of BC TOA DRF to aerosol vertical redistribution.
Sensitivity of clear-sky BC TOA DRF to the assumed aerosol vertical profile for high-loading, strongly absorbing cases over Xuzhou and Dhaka. The top panels compare the probability-density distributions of BC TOA DRF from the baseline boundary-layer SBDART configuration and the elevated-layer sensitivity configuration. The middle panels show the absolute difference, |ΔBC TOA|, and the relative difference, $|\Delta BC\ TOA/BC\ TOA_{BL}|\times100$, between the two simulations. The bottom panel shows the empirical cumulative distribution function of the relative BC TOA DRF change. Column-integrated AOD, SSA, and asymmetry factor were kept fixed between the baseline and elevated-layer simulations; therefore, the differences shown here isolate the effect of vertical redistribution alone.

However, there are some caveats in our approach to analyze the sensitivity of BC vertical layer impact on BC DRF. First, the fixed 2.0 km boundary layer threshold does not account for temporal and spatial variability in boundary layer height, and the elevated-layer parameterisation reflects the statistics of available CALIPSO overpasses rather than the full range of possible vertical structures. Despite these limitations, this analysis represents our best effort to observationally

constrain the sensitivity of BC TOA DRF to aerosol vertical structure within the available dataset. The CALIPSO-derived layer statistics provide the only spatially collocated, observation-based characterisation of aerosol vertical distribution feasible for the study regions and periods examined. Within this constraint, the sensitivity experiment suggests that the vertical profile assumption adopted in the RTM calculations is not expected to introduce a large uncertainty in the BC TOA DRF estimates reported in this study.

We have now clearly mentioned in Supplementary Section S1 Theoretical Concept of Santa Barbara DISORT Atmospheric Radiative Transfer Model (SBDART) :

"*In this study, SBDART used its default near-surface-dominant aerosol vertical distribution, with aerosol loading concentrated within the lower atmosphere/boundary layer and decreasing with altitude*."

We also expanded our Conclusion section highlighting:

"*Finally, vertical variability of BC remains unresolved, reflecting both methodological choices and the maturity of current observing systems. A companion CALIPSO-constrained sensitivity analysis over Xuzhou and Dhaka showed that the dominant aerosol layers are largely boundary-layer confined, and that redistributing high-BCAOD, low-SSA cases into CALIPSO-derived elevated layers produced only modest BC TOA DRF changes, with median relative differences below 1% and 95th-percentile differences below approximately 2% (Tiwari et al., 2026). This suggests that the baseline vertical-profile assumption is unlikely to dominate the BC TOA DRF uncertainty over these two regions, although the retrieval remains column-integrated and does not resolve the true vertical profile of BC extinction.*"

3. The study explicitly states that no observational product is available for direct validation and therefore uses COSMO-RTM output as the "reference truth." This treatment will incorporate unceratinties in the COSMO model in the ML framework, and the results only represent emulation accuracy rather than physical correctness. I suggest the authors validate the model using CERES fluxes with high BC loading or AERONET derived forcing efficient under high AAOD conditions.

Thank you for this important and constructive comment. First, we clarify that we use COSMO-RTM output as the reference target not because we treat it as unconstrained truth, but because the radiative forcing framework is already rigorously observation-constrained at multiple levels. In specific, the BC direct radiative forcing is not derived from prescribed climatological assumptions; instead, it is calculated from observation-constrained BC microphysical states, including dynamically retrieved BC core size, coating thickness (mixing state), column number concentration, and the associated wavelength-dependent optical properties (BCAOD, SSA, ASY) at multiple wavebands, that are directly propagated into the radiative transfer calculations. These have previously been shown to be broadly consistent with observations from particle sizers and aethalometers (Guan et al., 2026a,b) in addition to AERONET and TROPOMI across respective wavebands (Tiwari et al., 2023; Tiwari et al., 2025). In addition, the radiative transfer calculations use observation-based ancillary inputs including column water vapor, ozone, surface albedo, and atmospheric structure, rather than idealized prescribed profiles. Therefore, COSMO-RTM in this

study represents an observation-constrained physically based BC forcing framework rather than a purely free-running model product. For this reason, we used COSMO-RTM output as the reference target for machine-learning emulation, since the objective of the ML model is to reproduce this physically constrained BC radiative forcing framework at high spatial resolution rather than to learn unconstrained model behavior.

However, we fully agree that physical credibility is stronger when additional observations or observationally influenced calculations are used, in addition to emulation using the reference model. **While strict one-to-one validation of BC-specific forcing against external platforms is not physically feasible, the COSMO RTM BC TOA should still demonstrate observational consistency with independent measurements.**

First, we carefully considered the reviewer's suggestion to use CERES fluxes with high BC loading. However, CERES has three important limitations that make it less suitable for validating our BC-specific DRF. First, CERES provides total aerosol radiative effects and cannot isolate BC absorption from other absorbing or scattering components, even under high AAOD conditions. As previously mentioned, a subset of our solutions is constrained in full by MODIS-MAIAC AOD and this subset may possibly be able to make such a comparison, however a separate subset yields an AOD smaller than that from MODIS AOD, meaning that additional purely scattering aerosol is also found in the column, which would not allow a one-to-one comparison. Second, CERES has a ~20 km footprint, which is substantially coarser than our 5 km retrieval grid, meaning that direct comparison would require resampling and introduce significant representativeness errors over heterogeneous urban domains. Third, deriving DRF from CERES requires estimating pristine-sky fluxes under low/zero AOD assumptions. While this is a reasonable approach in some regions which have a clean background period of time each year, it would add considerable uncertainty in many of the regions studied here, which are persistently polluted. For these reasons, a strict one-to-one comparison between CERES TOA flux perturbations and our COSMO-RTM BC-only DRF would not be physically equivalent.

We therefore pursued the AERONET-based approach, which enables more targeted consistency checks using SSA and AAE constraints under BC-like absorption regimes, as detailed below.

We define forcing efficiency (FE) as TOA DRF per unit AAOD rather than per unit AOD because this comparison targets the radiative impact of absorbing aerosols like black carbon. For total aerosol direct radiative forcing, DRF/AOD is commonly used because total extinction controls the combined scattering and absorption perturbation. However, for BC-specific forcing, the relevant optical driver is a non-linear combination of absorption and scattering rather than total extinction alone. Normalizing by AOD would likely linearize the non-linear BC absorption with co-emitted scattering aerosol and other non-BC absorbing components, such as dust and brown carbon, thereby obscuring whether the model's BC-specific microphysics, column loading, and absorption efficiency are physically consistent with independent observational constraints. This point is to allow a more radiatively consistent comparison against independent observations, which use different assumptions about BC microphysics and hence different inverted radiative forcing calculations. Therefore, we use an absorption-normalized FE.

To address the reviewer's request for an independent observational constraint, we performed an AERONET-based consistency assessment over Dhaka, where Version 3 Level 2.0 inversion radiative forcing products are available. This analysis uses AERONET total-aerosol TOA forcing and

absorption optical depth to evaluate whether COSMO-RTM BC TOA forcing behaves consistently with independent column radiative observations under absorbing aerosol conditions. Since AERONET represents total aerosol forcing whereas COSMO-RTM isolates the BC component, and AERONET makes assumptions about particle size and mixing which are treated more flexibly by COSMO-RTM, the comparison is not designed as a strict 1:1 validation. Instead, we performed three complementary checks:

1. **Temporal consistency:** whether COSMO-RTM BC TOA DRF and FE capture the day-to-day variability of AERONET total-aerosol TOA DRF and FE.
2. **Regime-dependent behavior:** whether the COSMO-RTM BC TOA FE and AERONET TOA FE relationship strengthens under low-SSA, spectrally BC-like conditions, and whether the residuals are physically structured by based on the AERONET definitions of size $AAE_{440\text{-}870}$ and SSA_{440}, since their structure is less flexible with respect to these aspects, we still follow their format.
3. **Relative-scaling diagnostic:** whether the magnitude of COSMO-RTM BC TOA FE is consistent with the expected BC-to-total aerosol contribution. This final diagnostic is needed because correlation and slope changes demonstrate covariability and regime dependence, but do not by themselves define the appropriate magnitude of a BC-only forcing contribution relative to an AERONET total-aerosol product.

For Dhaka, where AERONET radiative forcing products are available, we temporally matched AERONET Version 3 Level 2.0 inversion retrievals (TOA DRF) with our observation-constrained BC retrievals within a 20 km radius of the station, with model grid values aggreagated by daily mean to match AERONET's temporal resolution. AERONET AAOD at 550 nm was derived from linearly interpolating AERONET's measured absorption at AAOD (440 nm and 870 nm) and AERONET's AAE from 440 nm to 870 nm, to calculate the AERONET FE, as:

$$FE_{AERONET} = \frac{Rad\_Forcing(TOA)}{AAOD_{550}}$$

representing total aerosol forcing efficiency from AERONET. For the COSMO-RTM side, BC FE was calculated as:

$$FE_{BC} = \frac{DRF_{BC}}{BCAAOD_{550}}$$

using COSMO-SBDART-derived BC TOA forcing and the corresponding BC absorption optical depth specifically calculated at 550nm

Temporal Consistency check:

Figure 2 compares the temporal and anomaly-based behavior of AERONET total-aerosol TOA and COSMO-RTM BC-TOA over Dhaka. The temporal evolution of daily DRF shows that both datasets capture a similar temporal structure, with stronger negative forcing clustered mainly during winter to pre-monsoon polluted periods and fewer/weaker forcing events around the post-monsoon season (Figure 4a). Despite this magnitude difference, the timing of enhanced and reduced forcing is broadly consistent between the two datasets. This temporal consistency is

further supported by the matched-day standardized anomaly comparison (Figure 4b). After normalizing each dataset relative to its own median and interquartile range, the TOA DRF anomalies show strong positive agreement, with Pearson R = 0.7 and Spearman ρ = 0.7, both significant at $p < 0.001$. The regression slope of 0.76 indicates that the two datasets capture similar relative TOA variability, although with somewhat reduced anomaly amplitude compared with AERONET, consistent with one being an area average and the other a geospatial point. In addition, 76.4% of matched days show same-sign anomalies, indicating that both datasets generally identify the same stronger- and weaker-forcing regimes.

A similar pattern is observed for TOA FE showing comparable and in some cases tighter temporal clustering of stronger and weaker FE values (Figure 4c), suggesting that COSMO-RTM BC TOA retains similar observed variability as AERONET with respect to TOA FE. The FE anomaly scatter confirms this behavior more directly (Figure 4d). The matched-day FE anomalies show strong positive correspondence, with Pearson R = 0.73 and Spearman ρ = 0.68, both significant at $p < 0.001$. The regression slope of 0.82 suggests that the model and AERONET are mostly consistent in terms of relative FE anomaly amplitude. Same-sign anomaly agreement is 71.6%, indicating that AERONET total FE and model BC FE fall on the same side of their respective median states for nearly three-quarters of matched days.

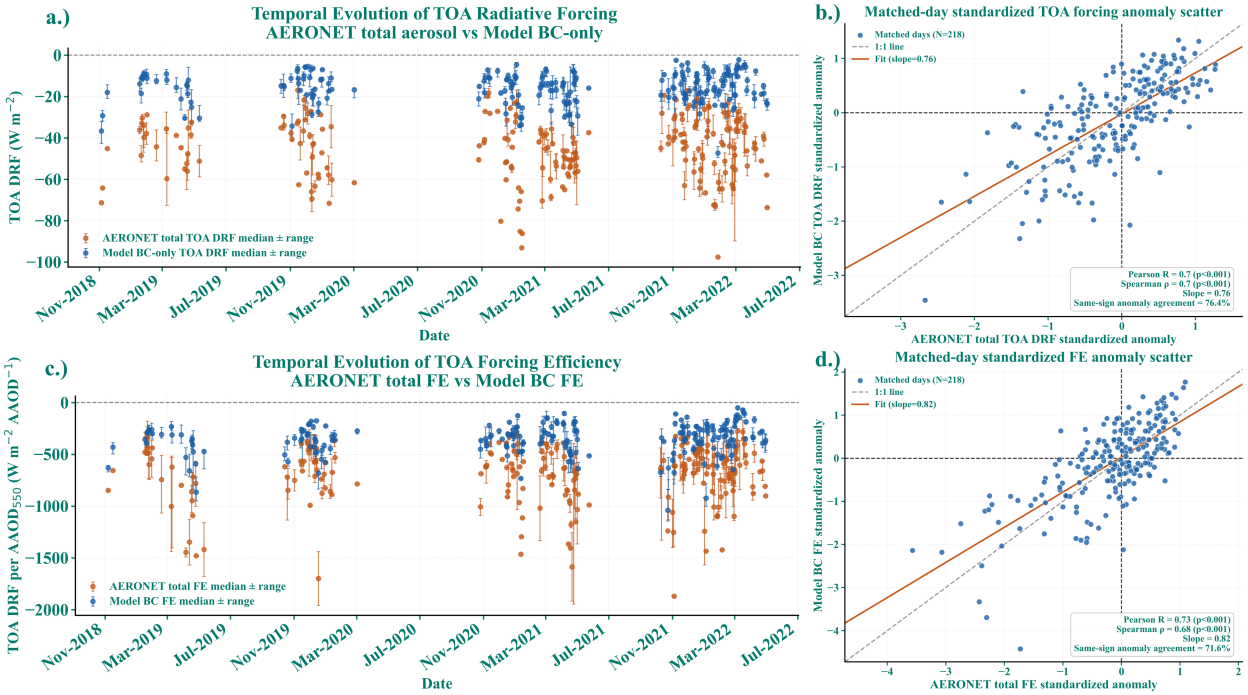

Figure 4: Temporal consistency between AERONET total-aerosol forcing and COSMO-RTM BC-only forcing over Dhaka.

(a,c) Daily temporal evolution of TOA DRF and TOA forcing efficiency from AERONET total-aerosol products and COSMO-RTM BC-only simulations. Points and bars show daily median and range. (b,d) Matched-day standardized anomaly comparisons for TOA DRF and TOA FE. The dashed line denotes the 1:1 reference and the solid line denotes the fitted regression. The comparison is used as an observational consistency check, not a strict one-to-one validation,

because AERONET represents total aerosol forcing while COSMO-RTM isolates BC-only forcing.

Overall, Figure 4 provides an initial observational consistency check showing that the model does not simply reproduce a static forcing response. In addition, it shows that the model captures similar temporal variability of both TOA DRF and FE. The systematic offset between COSMO-RTM BC-only values and AERONET total-aerosol values is physically expected because the two quantities do not represent the same aerosol component, the geospatial area, or using the same assumptions for aerosol size and mixing state. This motivates two follow-up tests: first, whether the model-AERONET FE relationship strengthens under more absorbing, spectrally BC-like regimes; and second, whether the observed scaling is consistent with the physically expected BC-to-total aerosol benchmark.

Regime-dependent strengthening of the COSMO-RTM and AERONET TOA FE relationship

We next examined whether the model-AERONET TOA FE relationship changes systematically with aerosol absorption regime (Figure 5a). Across all matched retrievals, the ordinary regression slope between $FE_{modelBC}$ and $FE_{AERONET}$ was 0.31, with a significant correlation (R = 0.6; p< 0.001) (Figure 5a). When the analysis was restricted to the conditions and, spectrally BC-like subset, defined by cases where SSA_{440} was below the 30th percentile and 0.8 < $AAE_{440\text{-}870}$ < 1.4 (Luo et al., 2023; Y. Liu et al., 2017) , the slope increased to 0.63 while the relationship remained significant (R = 0.55; p< 0.001). This increase indicates that the proportional scaling between COSMO-RTM BC FE and AERONET total-aerosol FE becomes closer under more BC-like absorption conditions.

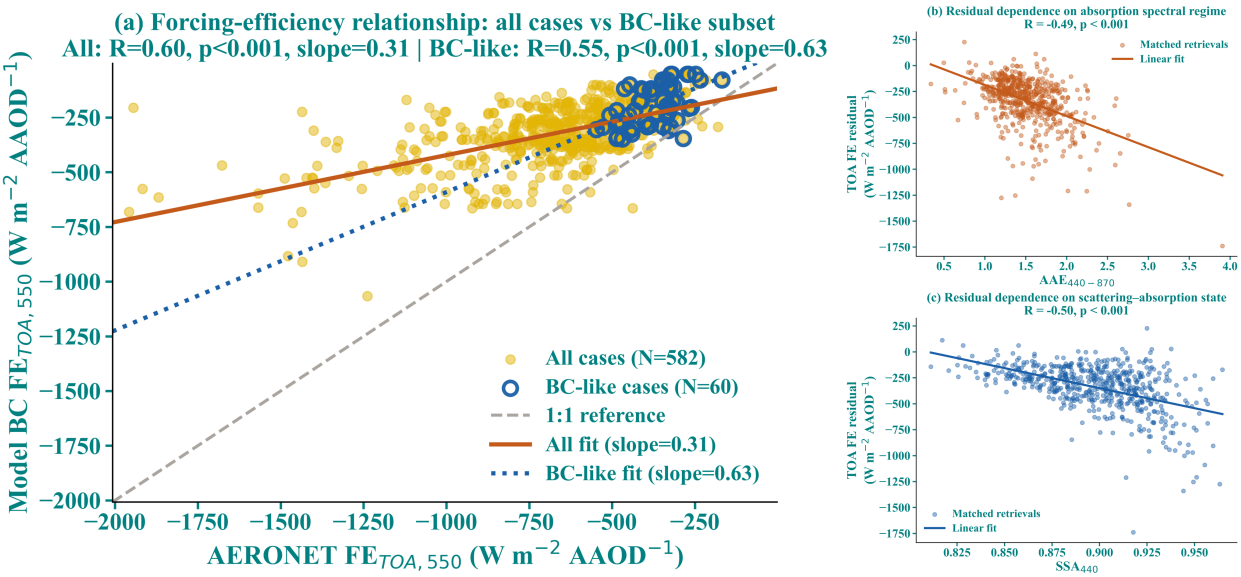

Figure 5: Regime-dependent consistency between COSMO-RTM BC TOA FE and AERONET total-aerosol TOA FE. (a) Scatterplot of COSMO-RTM BC-only TOA FE against AERONET total-aerosol TOA FE for all matched retrievals and for the spectrally BC-like subset. b) Residual dependence on AAE440-870. (c) Residual dependence on SSA440.

The residual analysis (Figure 5(b and c) further supports this regime dependence. The forcing-efficiency residual, is not randomly distributed with respect to aerosol optical state. Instead, it shows significant dependence on both $AAE_{440\text{-}870}$ and SSA_{440}. Residuals decrease systematically

with increasing AAE (R = -0.49; p< 0.001), indicating that the separation between AERONET total-aerosol FE and model BC-only FE changes as the absorption spectrum becomes less BC-like (Figure 5b). A similar but slightly stronger dependence is observed with SSA_{440} (R = -0.50; p< 0.001), showing that the residual structure is also controlled by the column scattering-absorption balance (Figure 5c).

Overall, the temporal consistency check indicated that COSMO-RTM BC TOA FE captures day to day variability of AERONET total-aerosol FE, indicating the model is not producing an unconstrained radiative response. Similarlly, regime-dependent analysis shows that the COSMO-RTM BC TOA FE and AERONET TOA FE relationship strengthens under low SSA and spectrally BC like conditions and the residuals are systematically structured by AAE and SSA. Together, these results demonstrate that the model-observation differences are partly organized by aerosol optical regime, rather than being structureless residual scatter.

However, the temporal and regime-dependent analyses primarily establish covariability and aerosol-regime structure. They do not by themselves determine whether the magnitude of COSMO-RTM BC TOA FE is quantitatively reasonable relative to AERONET total-aerosol TOA FE. This is in part impossible because AERONET makes the assumptions that AAE over 440nm to 870nm and a scaled SSA at 440nm are reasonable, while COSMO does not make that assumption, with the values of SSA and ASY computed from COSMO varying across the wavebands in a way which is more realistic than and more complex than using an angstrom exponent, consistent with new work elsewhere (Guan et al., 2026a,b; Tirpitz et al., 2026). Therefore, we next applied a relative-scaling test to define the appropriate BC-to-total aerosol benchmark and evaluate whether the observed model-AERONET FE magnitude falls within that expected range.

Relative scaling test

The theoretically expected TOA FE scaling derives from the ratio of two seperately computed fractions independent of the fitted FE regression. The **BC absorption fraction** quantifies BC's contribution to total column absorption at a single waveband (in this case 550nm):

$$R_{abs} = \frac{\text{BC AAOD}_{550}}{\text{AAOD}_{550}^{\text{AERONET}}}$$

The **BC forcing fraction** quantifies the magnitude of BC TOA forcing from COSMO-RTM relative to the AERONET total-aerosol TOA forcing:

$$R_{DRF} = \frac{\left|\text{DRF}_{\text{TOA,BC}}\right|}{\left|\text{DRF}_{\text{TOA,AERONET}}\right|}$$

If the COSMO-RTM BC microphysics and radiative-transfer calculation are physically consistent with the independent AERONET total-aerosol forcing constraint, then the observed scaling between FE_{BC} and $FE_{AERONET}$ should be consistent with:

$$\text{Expected TOA FE scaling} = \frac{R_{DRF}}{R_{abs}}$$

This expectation arises because the model BC FE represents radiative effect per unit BC absorption, while AERONET total FE represents radiative effect per unit total aerosol absorption. Their ratio therefore scales with the relative contribution of BC to both absorption and TOA forcing. Importantly, this expected scaling is not fitted from the FE regression itself; rather, it provides a physically constrained benchmark for evaluating whether the BC-only FE magnitude is

reasonable relative to the AERONET total-aerosol FE. It is therefore not a direct validation of isolated BC forcing, but a relative-scaling consistency test designed for the case where the observational product represents total aerosol forcing and the model isolates the BC component. Since this benchmark is a proportional ratio, it was compared with the origin-constrained COSMO-RTM TOA FE - AERONET total aerosol TOA FE slope, $FE_{BC} = mFE_{AERONET}$, rather than with the ordinary OLS slope that includes an intercept. The ordinary OLS slope was used above only to diagnose regime-dependent strengthening of the relationship.

Across all the matched retrieval, the median R_{abs} was 0.66 [95% CI: 0.62-0.69], indicating that BC accounts for approximately two-thirds of total column absorption in the matched Dhaka case at 550nm. This magnitude is consistent with previous global absorption-partitioning estimates; for example, Sand et al. (2021) reported that BC contributes about 60% of total aerosol absorption on average. The corresponding median R_{DRF} was 0.32 [0.29-0.35], indicating that COSMO-RTM BC TOA forcing accounts for approximately one-third of the AERONET total-aerosol TOA forcing magnitude. Together, these values yield an expected TOA FE scaling of 0.48 [0.44-0.53].

Table 1. Relative-scaling diagnostic between COSMO-RTM BC TOA FE and AERONET total-aerosol TOA FE.

Regime	R_{abs} [95TH CI]	R_{DRF} [95TH CI]	Expected TOA FE scaling [95TH CI]	Observed origin-constrained slope [95TH CI]	Median $FE_{BC}/FE_{AERONET}$
All cases	066[0.62-0.69]	0.32[0.29-0.35]	0.48[0.44-0.53]	0.46[0.43-0.48]	0.48
BC-like subset (SSA_{440} < 30th percentile and AAE 0.8-1.4)	0.51[0.45-0.57]	0.25[0.17-0.32]	0.50[0.33-0.62]	0.53[0.46-0.61]	0.55

Table 1 shows that the observed proportional COSMO-RTM BC TOA FE - AERONET total aerosol TOA FE scaling is consistent with the expected BC-to-total aerosol benchmark. For all matched cases, the observed origin-constrained slope was 0.46 [0.43-0.48], closely overlapping the expected scaling of 0.48 [0.44-0.53]. For the BC-like subset, the observed slope increased to 0.53 [0.46-0.61], while the expected scaling was 0.50 [0.33-0.62]. The median $FE_{BC}/FE_{AERONET}$ ratio also increased from 0.48 to 0.55 under BC-like conditions. Thus, the magnitude of COSMO-RTM BC-only TOA FE while is not expected to match AERONET total-aerosol TOA FE one-to-one, but it falls within the physically interpretable BC-to-total aerosol scaling range, especially considering that it is based only on the single 550nm waveband.

The decrease from 0.66 to 0.51 should not be interpreted as a weakening of the FE consistency result, because R_{abs} and R_{DRF} are both recomputed for a different optically filtered subset. The relevant diagnostic is not whether R_{abs} increases or decreases, but whether the ratio R_{DRF}/R_{abs} agrees with the observed origin-constrained FE slope. This agreement is maintained for both all cases and the more absorbing BC-like subset.

Concluding Remarks:

- COSMO-RTM BC TOA DRF and FE reproduce the relative day-to-day variability of AERONET total-aerosol TOA DRF and FE over Dhaka, indicating that the model does not produce a static or unconstrained radiative response.
- Regime-dependent behavior: The COSMO-RTM-AERONET TOA FE relationship strengthens under low-SSA, spectrally BC-like conditions. The ordinary regression slope increases from 0.31 for all matched cases to 0.63 for the BC-like subset, showing that BC-only FE explains a larger fraction of AERONET total-aerosol FE under absorbing BC-like regimes.
- The relative-scaling diagnostic shows that the magnitude of COSMO-RTM BC-only FE is consistent with the expected BC-to-total aerosol scaling. Across all matched cases, the observed origin-constrained slope was 0.46, closely matching the expected TOA FE scaling of 0.48.

While the above analysis does not constitute direct validation of BC-specific DRF, but it substantially reduces the concern that the target COSMO-RTM BC TOA that ML surrogate predict or are trained on, tracks independent AERONET temporal variability, strengthens under physically expected BC-like regimes, shows residuals organized by SSA and AAE, and falls within the expected BC-to-total aerosol FE scaling range. Therefore, the COSMO-RTM BC forcing framework is supported by independent observational consistency, not by ML emulation accuracy alone.

Note:

We were not able to replicate this AERONET forcing-efficiency analysis for Xuzhou. Since the transition of the Xuzhou site to the SONET system, there are no released total-aerosol DRF products available

We have added this analysis to the Supplementary Information as **Section S2**, titled **"AERONET-based consistency assessment of COSMO-RTM BC TOA forcing efficiency."** The new section includes the regime-dependent COSMO-RTM BC TOA-AERONET TOA FE comparison, residual dependence on AAE and SSA, and the relative-scaling diagnostic used to evaluate whether the BC-only FE magnitude is consistent with the expected BC-to-total aerosol contribution.

4. Only two sites, Xuzhou and Dhaka, were selected to validate the model, which in my opinion, is not sufficient to justify the transferability of the model. Both sites are polluted urban regions, but BC can be extensive at biomass burning regimes, some of which are remote forest regions. Please consider adding more validation sites with different aerosol types.

We thank the reviewer for this insightful and constructive comment. The previous findings in Tiwari et al., (2025) do demonstrate that these sites are quite different from each other, with one impacted heavily by primary emissions from lower efficiency combustion and the other impacted more substantially by long-range transported and aged urban emissions, as well as some local emissions which occur from higher efficiency combustion. However, the suggestion to test transferability beyond the two original yet vastly different mixed urban and light/heavy industrial sites was particularly valuable, as it prompted us to conduct additional zero-shot evaluations in

contrasting aerosol regimes. This exercise has strengthened the manuscript and helped us refine our claims regarding model transferability.

To explicitly address concerns about transferability to other environments, we evaluated the performance of the **combined ML model (ML**, trained exclusively on the Xuzhou + Dhaka dataset)** over two additional regions with fundamentally different dominant aerosol types:

Delhi, India (October-November 2024, post-monsoon period): A heavily polluted megacity strongly influenced by post-monsoon agricultural residue burning from the surrounding Indo-Gangetic Plain, mixed with urban and industrial emissions. This period corresponds to the well-documented peak of crop-residue burning influence on Delhi's air quality (Mangaraj et al. 2025; Venkataraman et al., 2024). The introduction of agricultural emissions is unique to this area, as well as the topography contributing to pooling and trapping of the atmosphere, quite distinct from the other two urban/industrial sites.

Mongu, Zambia (July-October, 2024, dry-season): A remote site in southern Africa representative of intense biomass burning emissions during the peak dry season, and relatively clean conditions other times of the year. Mongu is a long-term AERONET site frequently used to characterize southern African savanna fire emissions (Eck et al. 2013). This area has very intense combustion during the burning period, with a very high fire radiative power and fires occurring in all directions around the observational site, leading to a very different profile than the other areas studied.

For both regions, **we independently repeated the full observational constraint workflow multi-wavelength SSA constraint (TROPOMI (388nm) + AERONET (440-1020nm)), total AOD filtering (MAIAC (470, 550nm) + TROPOMI (388nm)), thus deriving the BC microphysical and optical properties via the COSMO framework. Then we performed high-resolution SBDART radiative transfer simulations using consistent ancillary inputs.** This yielded 23 days / 22,589 spatio-temporal pixels over Delhi and 34 days / 14,260 spatio-temporal pixels over Mongu for which fully consistent COSMO-RTM BC TOA DRF values were generated. We then used the predictor values as input in the ML** and generated ML derived BC TOA for the two regions and compared the results with COSMO-RTM BC TOA. Results of the zero-shot transferability test are presented in the new Figure 6.

Zero-shot Evaluation Test

ML** transfers well to Delhi (Adj. R^2 = 0.91, RMSE = 2.3 W m^{-2}, MAE = 1.9 W m^{-2}, MBE = -1.7 W m^{-2}), demonstrating effective generalization to a heavily polluted urban-influenced environment during a period when the aerosol loading is significantly influenced by surrounding agricultural burning. Performance at Mongu, however, degrades substantially (Adj. R^2 = 0.83, RMSE = 4.4 W m^{-2}, MAE = 4.2 W m^{-2}, MBE = -4.2 W m^{-2}), with a systematic underprediction bias more than twice that observed at Delhi. The Adj. R^2 of 0.83 indicates that ML** correctly tracks the relative variability in BC TOA DRF. However, the MBE of -4.2 W m-2 reveals systematic underprediction bias, i.e. the model consistently underpredicts BC DRF magnitude.

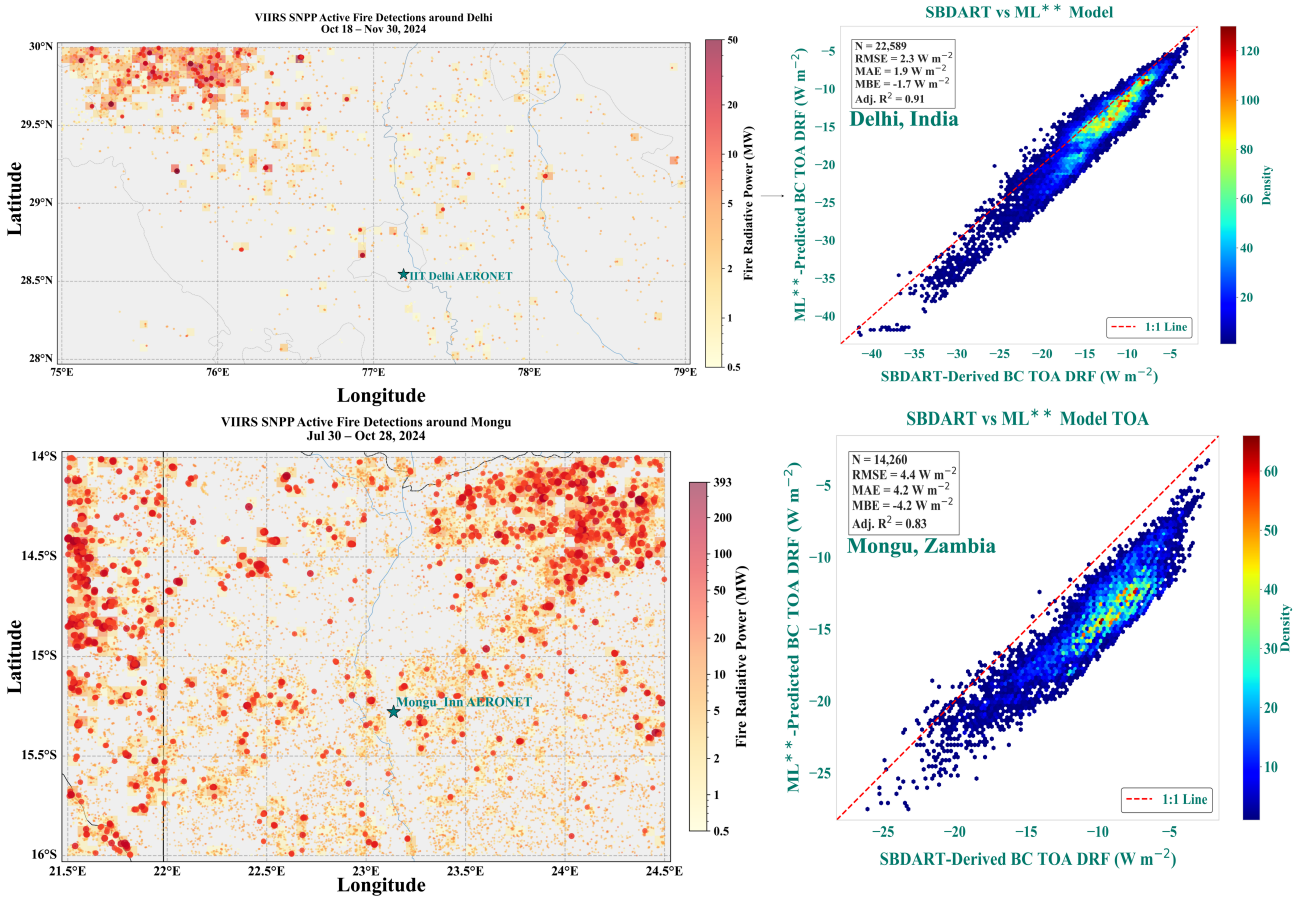

Figure 6. Zero-shot transferability evaluation of the combined ML model (trained exclusively on Xuzhou and Dhaka data) over two contrasting biomass burning-influenced regions. Left panels show the spatial distribution of VIIRS SNPP active fire detections (fire radiative power in MW) during the study periods, with the location of the local AERONET station marked by a star. Right panels show the comparison between SBDART-derived BC TOA DRF (reference) and ML**-predicted BC TOA DRF. Density scatterplots include key performance metrics (sample size N, RMSE, MAE, MBE, and adjusted R^2). Top row: Delhi, India (October - November, 2024), a complex urban-agricultural burning environment. Bottom row: Mongu, Zambia (August-Ocotber, 2024), a remote savanna biomass burning site.**

The contrasting performance between the two out-of-domain sites admits two interpretations: either ML** fundamentally fails to capture predictor and BC TOA relationship in new aerosol environments, or the degradation arises from a distributional mismatch where the test site's features fall outside the training domain. Distinguishing these possibilities is critical for assessing model limitations and guiding improvements. We address this through the feature-space overlap analysis.

Feature Space overlap Analysis

Feature-space overlap analysis compares the distribution of all five key ML** predictors (BCAOD550, N_c, BCsize, mixing-state, M_c) between the ML** training dataset and each test region (Delhi, Mongu), using the fraction of test samples within the training 2nd - 98th percentile range, Cohen's d effect sizes, and interquartile range overlap as diagnostic metrics.

For Delhi, all five predictors show > 97% overlap with the training distribution, with Cohen's d values uniformly below 0.30 and strong IQR overlap across all variables. This confirms near-complete distributional compatibility between Delhi and the Xuzhou + Dhaka training data. The model is interpolating within its learned feature space, which directly explains the strong zero-shot performance. The mixed urban-industrial emission along with agricultural burning influenced aerosol regime of Delhi during the post-monsoon period, while geographically distinct from the training sites, occupies essentially the similar microphysical and optical parameter space that ML** encountered during training. For Mongu, the overlap analysis reveals a systematic, multi-predictor distributional mismatch across the key predictors. Sulfate size (which impacts the mixing state) shows the most severe divergence (60.7% overlap, Cohen's d = -2.83), followed by Nc (80.8% overlap, Cohen's d = +1.18), BCsize (84.2% overlap, Cohen's d = -1.67), and Mc (88.3% overlap, no IQR overlap). The seemingly high 88.3% overlap in Mc is driven solely by the distributional tails, whereas the zero IQR overlap reveals that the bulk of Mongu's aerosol mass loading occupies a range entirely disjoint from the training data's central tendency. The mixing-state predictor reveals similar diagnostic. Despite 99.2% overlap with the training range, Cohen's d = +1.02 indicates a large systematic shift. This apparent contradiction is physically interpretable as mixing_state = BC size/total size can yield numerically similar ratios from fundamentally different microphysical configurations. In Mongu, the higher mixing-state arises from a small BC core (~103 nm) with a thin coating (~203 nm). In the training data, a similar ratio corresponds to a larger core (~120 nm) with proportionally thicker sulfate coating (~480 nm). The ratio overlaps numerically, but the underlying particle architecture and thus the radiative behavior, is physically distinct. This mismatch is invisible to aggregate overlap metrics but captured by Cohen's d, explaining why these predictors may contribute to systematic underprediction at Mongu despite its high percentile overlap.

These results raise a critical question: are the Mongu retrievals (as derived from COSMO as large number column abundance of thinly coated small BC particles) physically representative of southern African savanna fire aerosol? If the retrievals are unreliable, the feature-space divergence signals a methodological flaw; if they are physically realistic, it signals a solvable training coverage problem.

Physical Interpretation and Validation of COSMO Retrievals for Mongu

The COSMO-retrieved BC core median size for Mongu (~103 nm) is smaller than the training dataset median used in ML** (Xuzhou+Dhaka). This is consistent with savanna fire BC particles which are emitted close to the source, in every direction, and hence regardless of the wind direction there is a substantial amount of freshly combusted BC that has in turn undergone less coagulation and in-situ growth compared to relatively more aged urban BC characteristic of Xuzhou and Dhaka. In-situ SP2 measurements of African biomass burning smoke consistently report BC core count median diameters in the range of ~100–200 nm, with values varying by transport age and fire type (Wu et al., 2021). The Mongu retrieval falls squarely in the middle of

this range, as expected for a regional receptor site dominated by fresh to moderately aged savanna smoke.

The retrieved median coating thickness is ~203 nm at Mongu versus ~432 nm in the training data, i.e., coatings ~53% thinner than those typical of urban BC. This aligns with the low sulfate burden and constrained secondary organic aerosol accumulation in remote southern African savanna environments, where industrial sulfur emissions are minimal. SP2-based measurements of West African savanna fire plumes report median BC coating thicknesses increasing from ~13 nm at the source to ~50 nm after approximately 12 hours of atmospheric transport, reflecting the limited coating accumulation characteristic of flaming-controlled biomass burning (Wu et al., 2021). For broader context, laboratory and field studies of biomass burning smoke have reported core-shell coating growth factors of approximately 1.45, corresponding to coating thicknesses of around 32 nm, though these estimates derive from temperate forest fire conditions rather than African savanna fires (Lack et al., 2012). These are substantially thinner than the relatively thick, chemically processed coatings characteristic of urban-influenced BC in the training dataset. The lifecycle of biomass burning aerosol coatings further supports this, with rapid initial growth followed by slower accumulation or net loss with continued ageing (Sedlacek et al., 2022), keeping coatings thinner relative to urban pollution. Study by Wang et al., (2025) has shown that this area has a very high amount of NO_x emitted during this time, which would provide a way through co-emitted NO_x to rapidly form nitrate aerosols, which are optically identical to sulfate, and hence could fill the gap between the thinner shell sizes observed using COSMO and the even thinner shell sizes from the above observational studies.

The higher mixing state at Mongu directly reflects this thinner coating regime. In this study higher values of mixing-state indicate that the BC core constitutes a proportionally larger fraction of total particle volume, corresponding to a less internally mixed, less chemically aged aerosol population, also consistent with the shorter transport range from the fires to the AERONET site. This is the expected microphysical signature for savanna fire BC at a receptor site, the BC core remains dominant because sulfate condensation and organic coating accumulation are limited compared to heavily polluted urban environments (Wu et al., 2020, 2021; Lack et al., 2012), and only enhanced NO_x emissions are likely contributing (Wang et al., 2025; J. Liu et al., 2024b). In biomass burning smoke, a large fraction of organic material can also remain externally mixed, further preserving a higher effective mixing state relative to urban aerosols.

The elevated column N_c at Mongu is consistent with the high particle number densities characteristic of optically thick dry-season southern African smoke plumes. Dense savanna fire emissions continuously produce substantially higher number concentrations (Wu et al., 2020; Holanda et al., 2020) than the more diffuse urban pollution fields of Xuzhou and Dhaka.

Critically, the COSMO framework imposes no a-priori assumptions about aerosol source type. The retrieved BC core size, mixing state, and number and mass column density emerge purely from the requirement that core-shell Mie parameters simultaneously reproduce the observed multi-wavelength SSA (TROPOMI 388 nm, AERONET 440-1020 nm) and are again constrained by total AOD (TROPOMI 388 nm, MAIAC 470 and 550 nm) within measurement uncertainties. The strong independent agreement between these observation-driven microphysical retrievals and in-situ SP2 measurements of southern African savanna fire aerosol (Wu et al., 2020, 2021) provides independent physical support for the plausibility of the COSMO-retrieved Mongu microphysical regime. It confirms that the retrieved properties at Mongu represent a physically

realistic and distinct aerosol regime rather than a retrieval artifact. Consequently, the observed feature-space divergence from the training data is a genuine signature of savanna fire BC-an aerosol type underrepresented in the ML training, thus offering a physically grounded and statistically rigorous explanation for the systematic underprediction at this site.

ML** Model Revision: Incorporating Biomass Burning Regimes into Training

To improve transferability, we retrained the combined model (ML**; trained on Xuzhou +Dhaka) to revised combined model (ML***) by expanding the training dataset to include Delhi and Mongu alongside Xuzhou and Dhaka. This allows the model to learn the distinct microphysical signatures of biomass burning aerosol specifically, smaller BC cores, thinner coatings, and higher number concentrations combinations that were under-represented in the original training data. 70% of the data from each region was used for training (Xuzhou: 73,898; Dhaka: 191,258; Delhi: 15,813; Mongu: 9,982; total: 290,952 samples). The remaining 30% from each region (Xuzhou: 31,671; Dhaka: 81,967; Delhi: 6,776; Mongu: 4,278; total: 124691 samples) was held out as a test set, that was completely unseen during model training.

To prevent overfitting and ensure robust generalization, we further split the 70% training data from each region into an internal training set (80%) and a internal test set (20%). The validation set was used solely to monitor model performance during training and to detect signs of overfitting - specifically, divergence between training and internal test metrics. No information from the held-out test set (30% from each region) was used at any stage of model development, hyperparameter tuning, or validation. The internal validation showed minimal gap between training and validation performance (R^2 difference < 0.005; RMSE difference < 0.05 W m-2), indicating no overfitting. The final model was then evaluated exclusively on the completely unseen held-out test data (Figure 7).

On the completely unseen held-out test data, ML*** achieved strong and consistent performance across all four regions. For the urban sites, Xuzhou (N = 31,670) yielded Adj. R^2 = 0.95, RMSE = 2.0 W m^{-2}, and MBE = -0.2 W m^{-2}; Dhaka (N = 81,967) yielded Adj. R^2 = 0.95, RMSE = 1.7 W m^{-2}, and MBE = +0.2 W m^{-2}. For the biomass burning-influenced site, Delhi (N = 6,776) achieved Adj. R^2 = 0.94, RMSE = 1.6 W m^{-2}, and MBE = -1.1 W m^{-2}; Mongu (N = 4,278) achieved Adj. R^2= 0.89, RMSE = 1.4 W m^{-2}, and MBE = -0.8 W m^{-2}. The near-identical performance between urban sites and the modestly lower but still robust performance at Mongu demonstrate that ML*** performs effectively across diverse aerosol regimes without degrading urban accuracy.

Finally, the ML*** was applied to the full datasets from all four regions and compared its performance against the original ML** model (combined model trained only on Xuzhou and Dhaka). **This assesses two questions: does adding biomass burning data improve performance at Mongu, which at the same time preserving the accuracy of the results in both of the different original urban areas of Xuzhou and Dhaka?**

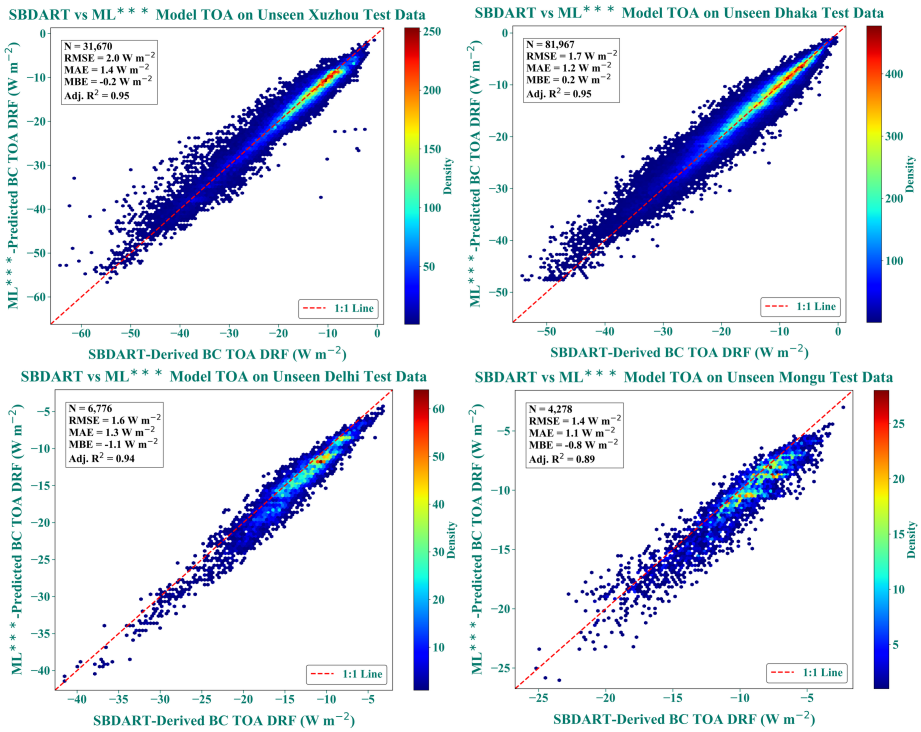

Figure 7. Performance of the revised combined model (ML*) on held-out test data across the four regions (30% from each region, 124,691 total samples, completely unseen during training). Panels show SBDART-derived vs ML*** predicted BC TOA DRF**

The results show that, urban performance remains virtually unchanged; Xuzhou and Dhaka show negligible differences, confirming that incorporating extreme biomass burning cases from Mongu and mixed urban-biomass burning cases form Delhi does not compromise the model's ability to capture urban BC-radiation interactions. ML*** substantially improves performance at the biomass burning-influenced sites. For Delhi, RMSE improves by 30% and bias reduces by 35%. For Mongu, RMSE decreases by 68% and bias improves from -4.2 to -0.8 W m-2. Consistent performance across region by ML*** demonstrates that the revised combined model transfers effectively across diverse aerosol regimes, from polluted urban environments with signatures of biomass burning (Xuzhou, Delhi, Dhaka) to remote savanna fire (Mongu) environments.

Table 2: Performance comparison between the original Xuzhou-Dhaka trained combined ML model (ML) and the revised four-region combined ML model (ML***) for predicting COSMO-RTM BC TOA DRF.**

Region	N	Model	Adj. R^2	RMSE (W m^{-2})	MBE (W m^{-2})
Xuzhou, China	**105,569**	**ML****	**0.96**	**1.9**	**-0.26**
		ML***	**0.96**	**1.9**	**-0.2**
Dhaka, Bangladesh	**273,225**	**ML****	**0.96**	**1.6**	**0.1**
		ML***	**0.95**	**1.6**	**0.2**
Delhi,	**22,589**	**ML****	**0.91**	**2.3**	**-1.7**

India		**ML*** **	**0.94**	**1.6**	**-1.1**
Mongu, Zambia	**14,260**	**ML** **	**0.83**	**4.4**	**-4.2**
		ML* **	**0.9**	**1.4**	**-0.8**

We have added this analysis to the main-text as **Section 3.6**, titled **"3.6 Diagnosing transferability limits: zero-shot evaluation on complex urban and biomass burning regions and improving ML****

Additionally we have now revised our conclusion section in regards to transferability of ML**. The revision on the conclusion sections are as follows:

Original Text:

Apparent transferability limitations emerge clearly in ML* applications, where systematic biases reflect mismatches in underlying aerosol microphysics rather than random error. These effects are substantially mitigated in the ML** model, which achieves error metrics comparable to, and in many cases lower than, region-specific ML and well below the inter-model spread reported for BCTOA DRF. As such, ML** can serve as a computationally efficient surrogate to augment under well-characterized aerosol regimes, and act in-situ for repeated RTM simulations required for regional BCTOA assessment. For practical deployment, two diagnostics are essential: (i) verifying overlap between the target region and training distributions of key predictors (e.g., BC core size, mixing-state, $BCAOD_{550}$, and N_c), and (ii) confirming consistency in dominant forcing drivers using SHAP attribution. Significant divergence in either indicates reduced transferability and the continued need for RTM benchmarking**.**

Revised Text:

"*Transferability tests over Delhi and Mongu show that ML surrogate performance depends strongly on how well the target aerosol microphysical and optical regimes are represented within the training feature space. The original Xuzhou-Dhaka-trained combined model (ML**) reproduced Delhi reasonably well, indicating that geographically distinct regions can still be predictable when their BC microphysical and optical predictors remain within the learned domain. In contrast, the systematic underprediction over Mongu reflected a distinct savanna-fire regime characterized by smaller BC cores and thinner coatings outside of the main ranges of the training dataset, as well as higher column number abundance near the top of the range of the training dataset, and shifted predictor distributions relative to the ML** training data. Incorporating Delhi and Mongu into the revised four-region model (ML***) substantially reduced this bias, particularly over Mongu, while preserving performance over Xuzhou and Dhaka, and slightly improving performance of Delhi. These results indicate that transferability is not universal, but is diagnosable and can be improved by expanding the RTM training ensemble to include underrepresented aerosol regimes. Therefore, surrogate deployment should be preceded by a quantitative feature-*

*space compatibility test. Simple inclusion within the training min-max range is not sufficient, because distributional tails can mask systematic shifts in the central predictor space. Instead, target-region predictors should be compared with the training domain using complementary diagnostics: (i) the fraction of samples within the training 2^{nd}-98^{th} percentile range, (ii) Cohen's d effect size to identify systematic distributional displacement, and (iii) interquartile-range overlap to determine whether the bulk of the target distribution lies within the learned regime. This also demonstrates that the traditional approach of prescribing fixed optical and microphysical properties for urban and biomass burning aerosol types - which global models currently heavily rely upon (Brown et al., 2021; Chen et al., 2023; Das et al., 2024) is likely incompatible with the diversity of microphysical properties revealed within each type by observationally constrained retrievals.***"***

We have also revised our abstract adding the new results as:

"*To test transferability, the combined ML model (trained in Xuzhou, China and Dhaka, Bangladesh) was evaluated zero-shot on two additional regions with contrasting aerosol microphysical conditions represented by Delhi, India (urban and agricultural burning sources) and Mongu, Zambia (strong savanna fires). While transference to Delhi is reasonable (Adj. R^2 = 0.91, RMSE = 2.3 W m^{-2}) there is a systematic underestimate at Mongu (Adj. R^2 = 0.83; MBE = -4.2 W m^{-2}). Feature-space overlap analysis attributes this degradation to a distributional mismatch in key microphysical predictors. Retraining on an expanded dataset including all four regions preserves urban performance while reducing Mongu RMSE by 68% and bias from -4.2 to -0.8 W m^{-2}.***"***

5. The interpretation of SHAP results may be over physical. SHAP only provides correlative behaviors in the model, not physical causality. Claims such as "BCAOD sign reversal", "mixing state controls warming vs cooling" should be weakened.

We thank the reviewer for this important clarification. We agree that SHAP analysis should not be over-interpreted as independent evidence of physical causality. SHAP identifies model-attribution patterns and predictor associations, rather than **directly revealing the underlying causal physical mechanisms**. The ML model is trained to reproduce the COSMO-RTM derived BCTOA values, and SHAP is used only as a diagnostic tool to interpret how the trained surrogate distributes prediction contributions among the input variables.

Following the reviewer's suggestion, we have revised the SHAP discussion to avoid language implying that SHAP independently proves physical causality. Specifically, we now describe SHAP results as **model-attribution patterns**, **surrogate-model sensitivities**, or **associations between predictors in estimating BC TOA DRF**, rather than as direct causal mechanisms. We also revised phrases such as "BCAOD sign reversal" and "mixing state controls warming versus cooling" to clarify that these refer to changes in the **sign of SHAP attribution** within the trained model, not to isolated physical perturbations of BCAOD or mixing state.

Abstract:

Original text:

Predictor decomposition reveals BCTOA is primarily modulated by BC aerosol optical depth (BCAOD), column number density, and mixing state, with their relative importance and influence varying non-linearly across cooling-to-warming regimes.

Revised text:

SHAP-based predictor attribution indicates that BCTOA estimates are most strongly associated with BC aerosol optical depth (BCAOD), column number density, and mixing state, with their relative contributions varying non-linearly across cooling-to-warming regimes.

Section 3.3:

Original text:

To interpret and quantify the contribution of individual predictors to the BCTOA radiative forcing, we applied Shapley Additive exPlanations (SHAP) analysis. This analysis provides a model-agnostic measure of how variations in BC optical, microphysical, and column properties influence the predicted TOA forcing under contrasting atmospheric and emission environments in Xuzhou and Dhaka (Figure 5), while explicitly accounting for non-linear feature interactions.

Revised text:

To interpret how the ML surrogate reproduces COSMO-RTM-derived BC TOA, we applied SHAP analysis to decompose the model predictions into feature-level attributions (Figure 5). This provides a diagnostic of how BCAOD550, column number density, mixing state, BC size, and column mass contribute to predicted BCTOA across Xuzhou and Dhaka.

Original Text:

In this context, the present SHAP analysis further also reveals that per-particle microphysics and overall column loading can each contribute may also strongly associate with either positively or negatively to TOA forcing, depending on their coupled state.

Revised Text:

In this context, the SHAP analysis further shows that variability in per-particle microphysics and column loading contributing to BCAOD variability do not map onto a single TOA response, instead depending on their coupled state, they are associated with either positive or negative contributions to predicted BCTOA.

Original text:

This sign change in SHAP association, likely, reflects a transition in the modeled radiative response…

Revised text:

This sign change in SHAP likely reflects a transition in the modeled radiative response

Original text:

In this context, the present SHAP analysis further reveals that per particle microphysics and overall column loading can each contribute either positively or negatively to TOA forcing, depending on their coupled state.

Revised text:

In this context, the SHAP analysis further shows that per-particle microphysics and column loading do not map to a single TOA response, instead depending on their coupled state, they are associated with both positive or negative contributions to predicted BC TOA.

Original text:

…with only the upper ~31% of column mass loading (>450 mg m^{-2}) contributing to cooling

Revised text:

…with only the upper ~31% of column mass loading (>450 mg m-2) associated with cooling in the model prediction.

Conclusion:

Original text:

SHAP analysis further reveals that BC radiative forcing is governed by strong non-linear interactions among…

Revised text:

SHAP analysis of the trained surrogate further indicates that model learns parametrization, in which the predicted BC TOA DRF depends strongly on non-linear interactions among….

Minor Comments:

1. Terminologies are not clear. “BCTOA”, “TOA forcing”, “BCTOA DRF” are used interchangeably; “mixing state” is sometimes defined, sometimes assumed; “Cooling-to-warming regimes” and “TOA regimes” are introduced informally and not rigorously defined.

We thank the reviewer for highlighting these inconsistencies. We have implemented the following clarifications throughout the manuscript:

(1) BC TOA , BC TOA DRF and TOA: We confirm that BC TOA and BC TOA DRF are used interchangeably to denote black carbon top-of-atmosphere direct radaitive forcing, unless otherwise stated. The standalone abbrevation TOA is now reserved exclusively for general references to the top of the atmosphere (TOA) (e.g. “aerosol direct radiative forcing at the top of the atmosphere (TOA)”). A disclaimer to this effect has been added in the introduction to prevent any confusion.

(2) Mixing state was defined in line 234 in the Method as ratio of BC core size to total size. Higher mixing state are proxy for large BC cores which are relatively less coated, while lower mixing state are proxy of aged BC particles.

(3) We agree that these regimes were introduced informally in the original manuscript. They are now formally defined in Section 2.2 (immediately following the pollution and

morphological regime categorization), where the stratified model-testing framework is established. The revised text reads:

" *Similarly, BC TOA forcing regimes, characterizing the transition from strong cooling to warming effects were defined by stratifying SBDART-derived BC TOA ensemble for both the regions into percentile-based categories. Low BC TOA (strong cooling, ≤25th percentile), Mid-Low BC TOA (25th-50th percentile), Mid-High BC TOA (50th-75th percentile), and High BC TOA (warming, ≥75th percentile).*"

2. Typos: Missing spaces (e.g., "AOD550values"); Repeated words ("also also incorporate"); Inconsistent units formatting (e.g., W m-2 vs. W m^{-2}).

We thank the reviewer for this careful reading. We have tried our best to proof read the mansucript and correct the typographical and formatting inconsistencies. Specifically:

i.) Missing spaces have been inserted
ii.) Instances of repeated words, including "also also incorporate" (line 73), have been removed ; and
iii.) Unit formatting has been standardized to W m^{-2}

3. Several figures, such as Figures 3 and 4, are overcrowded and the fonts are too small.

We thank the reviewer for this constructive observation. To reduce overcrowding and improve legibility, we have relocated panels **h)** and **i)** from Figure 3 to the Supplementary Information (see new Supplementary Figure S3), where the core-shell size distributions are presented with enlarged axes and labels. The main-text Figure 3 now retains panels **a)** through **h)**, allowing the probability density distributions of the key predictors to be displayed at a larger scale. Additionally, both Figure 3 and Figure 4 have been regenerated at higher resolution with substantially increased font sizes for all axis labels, tick marks, and legends to ensure clarity.

4. Please add 1:1 line, and statistics (Bias, RMSE) to Figure 4.

We appreciate this helpful suggestion. We have revised Figure 4 to include **1:1 reference lines** in all scatter-density panels (a-f), enabling immediate visual assessment of how closely each surrogate model (Linear, MLR, and ML) tracks the SBDART-derived BC TOA benchmark. Furthermore, we have added **performance statistics**-including Bias, RMSE, MAE, MAPE and Adj. R^2 directly as insets within each corresponding panel. The figure has been regenerated at higher resolution with enlarged fonts to ensure that all statistical annotations and the 1:1 line are clearly legible.

References:

Ahlberg, E., Ausmeel, S., Nilsson, L., Spanne, M., Pauraite, J., Nøjgaard, J. K., Bertò, M., Skov, H., Roldin, P., Kristensson, A., Swietlicki, E., & Eriksson, A. (2023). Measurement report: Black carbon properties and concentrations in southern Sweden urban and rural air – the importance of long-range transport. *Atmospheric Chemistry and Physics*, *23*(5), 3051–3064. https://doi.org/10.5194/acp-23-3051-2023

Eck, T. F., Holben, B. N., Reid, J. S., Mukelabai, M. M., Piketh, S. J., Torres, O., Jethva, H. T., Hyer, E. J., Ward, D. E., Dubovik, O., Sinyuk, A., Schafer, J. S., Giles, D. M., Sorokin, M., Smirnov, A., & Slutsker, I. (2013). A seasonal trend of single scattering albedo in southern African biomass-burning particles: Implications for satellite products and

estimates of emissions for the world's largest biomass-burning source. *Journal of Geophysical Research Atmospheres*, *118*(12), 6414–6432. https://doi.org/10.1002/jgrd.50500

Guan, L., Cohen, J. B., Wang, S., Tiwari, P., Liu, Z., Li, Z., & Qin, K. (2026a). In-tandem multi-waveband particulate absorption and size observations yield substantial changes in radiative forcing over industrial Central China. *Atmospheric Chemistry and Physics*, *26*(4), 3107–3123. https://doi.org/10.5194/acp-26-3107-2026

Guan, L., Cohen, J. B., Wang, S., Tiwari, P., Liu, Z., & Qin, K. (2026b). Improving aerosol absorption estimates via Size-Resolved Constraints based on AERONET and in situ measurements. *Geophysical Research Letters*, *53*(5). https://doi.org/10.1029/2025gl117418

Holanda, B. A., Pöhlker, M. L., Walter, D., Saturno, J., Sörgel, M., Ditas, J., Ditas, F., Schulz, C., Franco, M. A., Wang, Q., Donth, T., Artaxo, P., Barbosa, H. M. J., Borrmann, S., Braga, R., Brito, J., Cheng, Y., Dollner, M., Kaiser, J. W., . . . Pöhlker, C. (2020). Influx of African biomass burning aerosol during the Amazonian dry season through layered transatlantic transport of black carbon-rich smoke. *Atmospheric Chemistry and Physics*, *20*(8), 4757–4785. https://doi.org/10.5194/acp-20-4757-2020

Huang, X., Gao, R. S., Schwarz, J. P., He, L., Fahey, D. W., Watts, L. A., McComiskey, A., Cooper, O. R., Sun, T., Zeng, L., Hu, M., & Zhang, Y. (2011). Black carbon measurements in the Pearl River Delta region of China. *Journal of Geophysical Research Atmospheres*, *116*(D12). https://doi.org/10.1029/2010jd014933

Huang, X., Sun, T., Zeng, L., Yu, G., & Luan, S. (2012). Black carbon aerosol characterization in a coastal city in South China using a single particle soot photometer. *Atmospheric Environment*, *51*, 21–28. https://doi.org/10.1016/j.atmosenv.2012.01.056

Lack, D. A., Langridge, J. M., Bahreini, R., Cappa, C. D., Middlebrook, A. M., & Schwarz, J. P. (2012). Brown carbon and internal mixing in biomass burning particles. *Proceedings of the National Academy of Sciences*, *109*(37), 14802–14807. https://doi.org/10.1073/pnas.1206575109

Liu, J., Cohen, J. B., Tiwari, P., Liu, Z., Yim, S. H., Gupta, P., & Qin, K. (2024a). New top-down estimation of daily mass and number column density of black carbon driven by OMI and AERONET observations. *Remote Sensing of Environment*, *315*, 114436. https://doi.org/10.1016/j.rse.2024.114436

Liu, J., Cohen, J. B., He, Q., Tiwari, P., & Qin, K. (2024b). Accounting for NO_x emissions from biomass burning and urbanization doubles existing inventories over South, Southeast and East Asia. *Communications Earth & Environment*, *5*(1). https://doi.org/10.1038/s43247-024-01424-5

Liu, Y., Yan, C., & Zheng, M. (2017). Source apportionment of black carbon during winter in Beijing. *The Science of the Total Environment*, *618*, 531–541. https://doi.org/10.1016/j.scitotenv.2017.11.053

Liu, Z., Cohen, J. B., Wang, S., Wang, X., Tiwari, P., & Qin, K. (2024c). Remotely sensed BC columns over rapidly changing Western China show significant decreases in mass and inconsistent changes in number, size, and mixing properties due to policy actions. *Npj Climate and Atmospheric Science*, *7*(1). https://doi.org/10.1038/s41612-024-00663-9

Luo, J., Li, Z., Qiu, J., Zhang, Y., Fan, C., Li, L., Wu, H., Zhou, P., Li, K., & Zhang, Q. (2023). The simulated source Apportionment of light absorbing aerosols: Effects of microphysical properties of Partially-Coated Black Carbon. *Journal of Geophysical Research Atmospheres*, *128*(10). https://doi.org/10.1029/2022jd037291

Mangaraj, P., Matsumi, Y., Nakayama, T., Biswal, A., Yamaji, K., Araki, H., Yasutomi, N., Takigawa, M., Patra, P. K., Hayashida, S., Sharma, A., Dimri, A. P., Dhaka, S. K., Bhatti, M. S., Kajino, M., Mor, S., Khaiwal, R., Bhardwaj, S.,

Vazhathara, V. J., . . . Mor, S. (2025). Weak coupling of observed surface PM2.5 in Delhi-NCR with rice crop residue burning in Punjab and Haryana. *Npj Climate and Atmospheric Science*, *8*(1). https://doi.org/10.1038/s41612-025-00901-8

Reddington, C. L., McMeeking, G., Mann, G. W., Coe, H., Frontoso, M. G., Liu, D., Flynn, M., Spracklen, D. V., & Carslaw, K. S. (2013). The mass and number size distributions of black carbon aerosol over Europe. *Atmospheric Chemistry and Physics*, *13*(9), 4917–4939. https://doi.org/10.5194/acp-13-4917-2013

Sand, M., Samset, B. H., Myhre, G., Gliß, J., Bauer, S. E., Bian, H., Chin, M., Checa-Garcia, R., Ginoux, P., Kipling, Z., Kirkevåg, A., Kokkola, H., Sager, P. L., Lund, M. T., Matsui, H., Van Noije, T., Olivié, D. J. L., Remy, S., Schulz, M., . . . Watson-Parris, D. (2021). Aerosol absorption in global models from AeroCom phase III. *Atmospheric Chemistry and Physics*, *21*(20), 15929–15947. https://doi.org/10.5194/acp-21-15929-2021

Sedlacek, A. J., Lewis, E. R., Onasch, T. B., Zuidema, P., Redemann, J., Jaffe, D., & Kleinman, L. I. (2022). Using the Black Carbon particle mixing State to characterize the lifecycle of biomass burning aerosols. *Environmental Science & Technology*, *56*(20), 14315–14325. https://doi.org/10.1021/acs.est.2c03851

Tirpitz, J.-L., Brockway, N., Colosimo, S. F., Spurr, R., Christi, M., Hall, S., Ullmann, K., Natraj, V., Theys, N., Hair, J., Shingler, T., Weber, R., Zhu, R., Dibb, J., Moore, R., Wiggins, E., and Stutz, J. (2026). Retrieval of ultra-violet aerosol absorption from radiation measurements in young wildfire plumes, *EGUsphere [preprint]*, https://doi.org/10.5194/egusphere-2025-5541

Tiwari, P., Cohen, J. B., Wang, X., Wang, S., & Qin, K. (2023). Radiative forcing bias calculation based on COSMO (Core-Shell Mie model Optimization) and AERONET data. *Npj Climate and Atmospheric Science*, *6*(1). https://doi.org/10.1038/s41612-023-00520-1

Tiwari, P., Cohen, J. B., Lu, L., Wang, S., Li, X., Guan, L., Liu, Z., Li, Z., & Qin, K. (2025). Multi-platform observations and constraints reveal overlooked urban sources of black carbon in Xuzhou and Dhaka. *Communications Earth & Environment*, *6*(1). https://doi.org/10.1038/s43247-025-02012-x

Tiwari, P., Cohen, J. B., Kahn, R., Gao, H., Guan, L., Liu, Z., Lu, L., Wang, S., Zaman, S. U., Fan, C., Lolli, S., Li, Z., Dubovik, O., & Qin, K. (2026). Observation-constrained black carbon radiative forcing from multi-sensor and multi-spectral remote sensing reveals divergent forcing pathways over Asian urban agglomerates. *SSRN Electronic Journal*. https://doi.org/10.2139/ssrn.6604914

Venkataraman, C., Anand, A., Maji, S., Barman, N., Tiwari, D., Muduchuru, K., Sharma, A., Gupta, G., Bhardwaj, A., Haswani, D., Pullokaran, D., Yadav, K., Raman, R. S., Imran, M., Habib, G., Kapoor, T. S., Anurag, G., Sharma, R., Phuleria, H. C., . . . Singh, V. (2024). Drivers of PM2.5 episodes and exceedance in India: a synthesis from the COALESCE Network. *Journal of Geophysical Research Atmospheres*, *129*(14). https://doi.org/10.1029/2024jd040834

Wang, J., Wang, J., Cai, R., Liu, C., Jiang, J., Nie, W., Wang, J., Moteki, N., Zaveri, R. A., Huang, X., Ma, N., Chen, G., Wang, Z., Jin, Y., Cai, J., Zhang, Y., Chi, X., Holanda, B. A., Xing, J., . . . Ding, A. (2023). Unified theoretical framework for black carbon mixing state allows greater accuracy of climate effect estimation. *Nature Communications*, *14*(1), 2703. https://doi.org/10.1038/s41467-023-38330-x

Wang, S., Cohen, J. B., Guan, L., Lu, L., Tiwari, P., & Qin, K. (2025). Observationally constrained global NOx and CO emissions variability reveals sources which contribute significantly to CO2 emissions. *Npj Climate and Atmospheric Science*, *8*(1). https://doi.org/10.1038/s41612-025-00977-2

Wang, Y., Zheng, Z., Sun, Y., Yao, Y., Ma, P., Zhang, A., Zhu, S., Zhang, Z., Chen, X., Pang, Y., Wang, Q., Che, H., Ching, J., & Li, W. (2025). Improved representation of black carbon mixing structures suggests stronger direct radiative heating. *One Earth*, *8*(5), 101311. https://doi.org/10.1016/j.oneear.2025.101311

Wu, H., Taylor, J. W., Szpek, K., Langridge, J. M., Williams, P. I., Flynn, M., Allan, J. D., Abel, S. J., Pitt, J., Cotterell, M. I., Fox, C., Davies, N. W., Haywood, J., & Coe, H. (2020). Vertical variability of the properties of highly aged biomass burning aerosol transported over the southeast Atlantic during CLARIFY-2017. *Atmospheric Chemistry and Physics*, *20*(21), 12697–12719. https://doi.org/10.5194/acp-20-12697-2020

Wu, H., Taylor, J. W., Langridge, J. M., Yu, C., Allan, J. D., Szpek, K., Cotterell, M. I., Williams, P. I., Flynn, M., Barker, P., Fox, C., Allen, G., Lee, J., & Coe, H. (2021). Rapid transformation of ambient absorbing aerosols from West African biomass burning. *Atmospheric Chemistry and Physics*, *21*(12), 9417–9440. https://doi.org/10.5194/acp-21-9417-2021